National Science Council Overseas Project
for Post Graduate Research

Corrosion Resistance Enhancement of Metal Using a
Graphene Film
Final Report

Report written by (same as the grantee):Chia Nan Shih

Project-associated (overseas) Advisor: Xueliang Sun

Research abroad destination (country/state):Canada/Ontario

Research abroad institute: Western University

Institute address: Mechanical and Materials Engineering

Western Engineering, Western University

London, Ontario, Canada, N6A 5B8

Also included in this report:

□Report of business trips, official visits, and workshop participations

□Report of international academic conference participations

A completion of this section is required for all grantees.
I acknowledge that I have read this project report and commented as follows: Project-associated advisor   Name (in full): Xueliang Sun Signature: Date(dd-mm-yyyy):
A completion of this section is only required for grantees of Ph.D. student level.
I acknowledge that I have read this project report. Comments (optional):   Domestic advisor   Name (in full):Ming Der Ger Signature: Date(dd-mm-yyyy):

摘要

石墨烯,二維 sp^2 鍵結碳結構,因為其具備優異電性、機械性能、化學穩定性等，被開發可望做為未來可繞電子元件。石墨烯主要的製備方式有:(1)機械剝離法，此方法難以量產供未來運用需求，(2)碳化矽裂解法，此方法需要在極高溫(1600℃)及高真空環境下操作，(3)氣相沉積法,最具有開發潛力的方法，但如何成長大面積且層數均勻之技術仍是一大難題。

此研究中，我們進行兩項主要研究:(1) 以石墨烯層做為不銹鋼之防蝕保護層(2)利用 Ni(carbon-buffering layer)及 TiSi₂(carbon-rejection layer)濺鍍金屬層改善不銹鋼表面石墨烯成長層數均勻性。

傳統的石墨雙極板有昂貴，笨重，體積龐大，不易攜帶等問題。不銹鋼具有質輕,機械強度高 ， 低成本等優勢，被視為取代石墨極板之潛力開發材料。但不銹鋼於燃料電池環境中易生成鈍化膜造成導電性下降之問題極需解決。電鍍鎳層於不銹鋼基材上，藉由鎳層緩衝不銹鋼與碳原子直接接觸反應，可於不銹鋼表面生成 100%覆蓋率之石墨烯層，電位極化測試及光學顯微鏡証明，石墨烯披覆之不銹鋼相較無石墨烯披覆之不銹鋼，顯示較佳之導電性及抗蝕能力。另外，亦可藉由改變 Ni(carbon-buffering layer)及 TiSi₂(carbon-rejection layer)厚度，調整不銹鋼表面石墨烯成長層數。

關鍵詞：石墨烯、氣相沉積法、金屬雙極板、防蝕鍍層

Abstract

Graphene, one-atom-thick two-dimensional layers of sp^2-bonded carbon structure, has been explored to be applications in flexible electronics because of the outstanding electrical, mechanical and chemical properties. The primary graphene preparartions are : (1) micromechanical cleavage of graphite, is difficult to scale up for applications. (2) thermal decomposition of a SiC substrate ,need ultra high temperature $(1600℃)$ and vacuum enviornment (3) chemical vapor deposition ,epitaxial growth on metal substrate is an promising alternative, but achieving large graphene domains with uniform thickness remains a challenge.

There are two main in this research: (1) growing graphene on stainless steel as a anti-corrosion coating. (2) tuning the layers of graphene on stainless steel substrate by adjusting the thickness of the Ni or $TiSi_2$ layer atop stainless steel.

The traditional graphite Bipolar plates (BPPs) have some disadvantages such as expensive, weight heavy, and volume massive, which bulky or heavy and carry inconvenience in the cell application. Because of the advantage of lightweight, high mechanical strength, and low cost, the stainless steel is considered a material to replace the traditional BPPs. But the stainless steel passive layer in a PEM fuel cell environment influence the electrical conductivity is eager to solve.

In this study, chemical vapor deposition (CVD) growth of graphene on a catalyzing Ni/SUS304 double-layered structure was investigated. The results indicated that the coverage of the surface by the deposited graphene was poor on the SUS304 substrate. However, when the stainless steel was pre-plated with a nickel catalyst layer, this layer contributed to the uniform catalysis of methane pyrolysis, thereby allowing the SUS304 stainless steel surface to be completely covered by multiple layers of graphene. In combination with potentiodynamic polarization and optical microscope, we demonstrate that graphene coated stainless steel has better conductivity properties and corrosion resistance than non-graphene coated stainless steel. In addition, tuning the layers of graphene on stainless steel substrate are achieved by tailoring the thickness of the Ni or $TiSi_2$ layer atop stainless steel.

keywords:graphene, chemical vapor deposition, metal bipolar plates , anticorrosion coating

1.Introduction

At present, most bipolar plates for fuel cells are made of graphite. Graphite is an excellent electrode material because of its low electrical resistance, resistance to corrosion, and physical and chemical stability. However, graphite is brittle and has poor mechanical properties; therefore, it cannot withstand use in mobile products or other applications involving vibrating environments. In addition, it is difficult to mechanically produce gas-flow channels in thin graphite plates, which can break during fuel-cell assembly. Therefore, to achieve the mechanical strength required during fuel-cell assembly, graphite bipolar plates must often be relatively thick; this requirement increases the weight and volume of fuel cells, limiting their applications and causing difficulties in the mass production of fuel cells[1]. Graphite bipolar plates represent more than 80% of the total weight and more than 45% of the total manufacturing costs for proton-exchange-membrane fuel cells[2]. If metals could be used to replace graphite bipolar plates, then the volumes and manufacturing costs of fuel cells could be significantly reduced[3].

Because of its low cost and good corrosion resistance, stainless steel is regarded as one potential material to replace graphite in bipolar plates. However, in the harsh environment of a fuel cell, a passive layer forms on the surface of stainless steel; this passive layer resists corrosion but increases the electrical impedance of the bipolar plates and lowers the power-generation efficiency of the fuel cell[4]. Many researchers have investigated how stainless steel surfaces might be modified with carbon materials to simultaneously satisfy the requirements of high corrosion resistance and low impedance. Cho et al. have used chromium carburization to form a chromium-carbon protective layer on the surface of stainless steel[5, 6]. However, when chromium powder reacts with carbon atoms to form chromium-carbon compounds, a chromium oxide layer readily forms, increasing contact resistance. The experiments of Wind et al. have demonstrated that gold-coated stainless steel exhibited the same properties as graphite plates in a 1,000-hour single-cell test; however, the high cost of gold poses a hindrance to the widespread use of gold-coated material[7]. Chung et al. have used an acetylene/hydrogen gas mixture to grow a graphite layer on a nickel/stainless-steel surface; during this process, the carbon atoms initially formed filamentous or spherical carbon structures on the nickel grain

boundaries[8]. Fukutsuka has used plasma-enhanced chemical vapor deposition (PECVD) to form a carbon film layer on stainless steel; however, the Raman spectrum of the carbon material grown in this manner clearly revealed structural defects[9]. Wang et al. have used a resin/carbon composite as a protective layer for stainless steel; however, the resin was not electrically conductive and increased the contact resistance of the bipolar plates[10].

In recent years, graphene has attracted a great deal of research attention because of its outstanding physical properties, such as its high electrical conductivity, high heat-transfer rate, and high specific surface area[11-16]. Various metal catalysts[17-20] and alloys[21-23] have been utilized to catalyze the decomposition of carbon source gases that cause carbon atoms to form single or multiple graphene layers on the metal surface during CVD. In the past, graphene nanofilms produced through CVD have primarily been used in transparent conductive films[24] and in transistors[25]. Recent studies have demonstrated that the properties of graphene include gas impenetrability[26-29] and oxidation resistance[30-32] so that it can be used as a protective layer on metal surfaces. Sreevatsa has used a modified chemical-mechanical polishing (CMP) method to adhere graphene to stainless steel[33]. Other researchers have used CVD to grow graphene on nickel and copper substrates[34-36]. Kang has used reduced graphene oxide as a protective layer to prevent the oxidation of metals[37]. Krishnamurthy has used graphene grown on porous nickel foam as electrodes in microbial fuel cells[38]. Some researchers have also reported that the coverage of copper plates with graphene could effectively reduce short-term air oxidation rates; however, structural defects in the graphene became channels through which oxygen could contact the copper surface, and thus the graphene coating accelerated the long-term oxidation rates of the copper surfaces[39, 40]. In 2014, Hsieh et al. used atomic layer deposition (ALD) to deposit aluminum oxide at graphene defects, thereby enhancing the corrosion resistance of graphene/Cu[41]. In the present study, we investigated the reactions of two stainless steel specimens, SUS304 and Ni/SUS304, with methane in a high-temperature environment. With a facile design involving a catalytic metal on stainless steel to control the carbon diffusion process, multiple protective layers of graphene with 100% surface coverage were grown directly on the stainless steel surface and provide excellent anti-corrosion properties and high conductivity.

Some scientists combine the differnet metal to synthesizing large-area monolayer,

bilayer and multilayer graphene films on Cu-Ni alloy foils by chemical vapor deposition with methane and hydrogen gas or solid carbon as precursors[34, 42]. The dissolution of carbons into nickel metals and their subsequent non-equilibrium precipitation cause the non- uniformity CVD graphene. With a suitable Ni–Mo alloy design, a facile control of graphene layer thickness could be achieved[21].

2.Results and discussion

2.1 Graphene on Stainless Steel as a High-Performance Anti-corrosion Coating

Raman spectra presented in Figure 1(a) indicate that a few layers of graphene (I_{2D}/I_G~0.5) were grown on both SUS304 and Ni/SUS304. In images of the actual specimens (Figure S1), the surface of the G/SUS304 specimen (Figure S1(b)) appeared dark gray, whereas the surface of the G/Ni/SUS304 specimen (Figure S1(c)) appeared silvery gray. Scanning electron microscopy (SEM) was used to examine the differences in the surface morphologies of the two specimens. Although the G/SUS304 specimen without pre-plated Ni exhibited a Raman signal indicative of graphene, Figures 2(a,b) present little visual evidence that the metal surface of this specimen was covered by graphene. By contrast, the surface of the G/Ni/SUS304-900-4hr specimen appeared to be completely covered by graphene (Figure 2(c-e)). In Figure 2(f), the red dashed lines indicate the boundaries of metal grains on the specimen surface, whereas the blue dashed lines indicate ripples associated with the graphene surface. It suggests that the graphene film grew continuously across the metal grain boundaries. Because of the large differences in the thermal-expansion coefficients of the metal and the graphene, ripples were generated in the surface of the graphene after rapid cooling. For comparison, Gullapalli and John et al. have used hexane and ethanol gas as reaction precursors for the growth of graphene films on stainless steel foil; however, these authors did not discuss the completeness of the graphene coverage or the distribution of the layers of graphene growth[43, 44]. We further examined the Ni/SUS304-900-4hr and SUS304-900-4hr specimens in a stepwise fashion by Raman mapping (size of mapping area: 40 µm × 40 µm). Figures 1(b) and 1(c) present the G-peak Raman mapping spectra for the G/SUS304-900-4hr and G/Ni/SUS304-900-4hr specimens, respectively. Figure 1(b) demonstrates that G/SUS304-900-4hr exhibited a weak G-peak signal (signal intensity:

<1000), and even in some spots signals were not detected; this finding indicates that there was a low degree of graphenization on the specimen surface. In contrast, Figure 1(c) reveals that the G/Ni/SUS304-900-4hr specimen exhibited an intense (signal intensity: 3000-8000) and continuous G-peak signal. The electroplated nickel layer of the Ni/SUS304 specimen played a buffering role by reducing the contact of the methane with the various metal elements in the stainless steel directly. From the Raman mapping in Figure 1(c) and the SEM image in Figure 2(e), it appears that, unlike the G/SUS304 specimen, the double-layered G/Ni/SUS304 specimen permitted the complete and continuous growth of a graphene layer on the stainless steel surface. Figure 1(d) demonstrates that the I_{2D}/I_G ratio for graphene was between 0.4 and 1.0, indicating that the stainless steel surface was covered by two or more layers of graphene. Multiple graphene layers and high graphene coverage can yield metals with excellent corrosion resistance[35, 45]. Figure 1(e) provides a high-resolution transmission electron microscopy (TEM) image of the G/Ni/SUS304-900-4hr specimen; the left side of this figure displays the clear orientation of the lattice on the surface of the stainless steel, and shows that the metal surface was covered by multiple graphene layers (marked with red lines). Figure 1(f) indicates that graphene could still grow on a metal surface that was not completely even, extending along the metal surface to provide a complete coating. The robust growth of the protective graphene coating explains why the underlying stainless steel surface of the Ni/SUS304-900-4hr specimen could be fully protected from corrosion and oxidation.

In addition, we observed an unusual phenomenon (presented in Figure 1(a)): after the Ni/SUS304 specimen had reacted with methane for 1 hour in a 900°C environment, it was difficult to detect Raman spectroscopy signals indicative of the carbon structure. Nickel is a strongly active metal and has high solubility of carbon that can readily catalyze the pyrolysis of carbon source gases. For these reasons, nickel has been widely used for the growth of graphene via CVD. In a high-temperature environment (900-1,000°C), the growth of single or multiple layers of graphene can occur on the surface of nickel foil after 5-10 minutes of reaction with methane[18]. However, there are large differences between the reaction mechanisms for the deposition of nickel on stainless steel and the mechanisms for the reaction between methane and nickel metal alone. Wang

et al. have proposed that under high-temperature conditions, a deposition reaction occurs between the carbon atoms in carbon steel and chromium powder to form chromium iron carbides, $(Cr, Fe)_xC_y$[46, 47]. The X-ray diffraction (XRD) results presented in Figure S2 demonstrate that after prolonged reaction with methane, a variety of metal carbides, consisting mainly of Cr_3C_2, Cr_7C_3, and Fe_2C, had formed on the surfaces of the G/SUS304-900-4hr and Ni/SUS304-900-4hr specimens. Because of the formation of the metal carbide components, after reacting with the methane the surface roughness of the SUS304 and Ni/SUS304 samples increased from 29 nm and 139 nm to 137 nm and 178 nm, respectively (Figure S3). We concluded that the reactions with the carbon source gas were only weakly catalyzed because SUS304 contains only 8~11% Ni (Table S1); after the pyrolysis of the methane, most of the available carbon atoms preferentially reacted with chromium and iron in the metal to form chromium iron carbides, whereas only an extremely small quantity of carbon atoms precipitated to form graphene. For this reason, the graphene film that was produced after 4 hours of reaction between SUS304 and methane gas was insufficient to completely cover the stainless steel surface (Figure 1(b)). By comparison, the nickel coating of the Ni/SUS304 increased the rate of reaction between the methane gas and the SUS304. Thus a graphene film that completely covered the stainless steel surface was observed (Figures 1(c) and 2(e)). In short, the Ni plating fulfilled two functions: (1) it acted as a barrier layer to slow the diffusion of carbon atoms into the stainless steel, lessening the formation of metal carbides and (2) its high catalytic activity and high carbon solubility increased the pyrolysis rate of the carbon source gas, resulting in the formation of multiple graphene layers that completely covered the stainless steel surface (see Figure 3 for the proposed mechanism)

We used both electrochemical and morphological analysis techniques to investigate the passivation effects on the tested specimens. The potentiodynamic polarization method was used to investigate corrosion phenomena for the SUS304, G/SUS304-900-4hr, and G/Ni/SUS304-900-4hr specimens in an electrolyte solution. The electrolyte selection was guided by the results of previous studies. In one such study, Prasai *et al.* used a mild electrolyte solution (0.1M $NaSO_4$) to conduct corrosion resistance tests[35]. Cl^-, SO_4^{2-}, CO_3^{2-}, PO_4^{3-}, and other anions can severely corrode metals/alloys; in particular, chloride

ions exhibit the strongest corrosion capabilities among these anions[45]. In the current study, we used a 3.5 wt. % NaCl solution to test the corrosion resistance of the graphene coating, which possesses a strong corrosive capability and simulates a marine environment. Figure 4(a) shows the polarization curves of the first scan. The corrosion potentials (E_{corr}) for the SUS304, G/Ni/SUS304-900-4hr, and G/SUS304-900-4hr specimens were 0.04 V, -0.15 V, and -0.32 V, respectively, whereas the corrosion currents (I_{corr}) for these three specimens were 1.49×10^{-7} A-cm^{-2}, 1.61×10^{-7} A-cm^{-2}, and 2.32×10^{-6}A-cm^{-2}, respectively. The corrosion currents remained relatively low for both the SUS304 and G/Ni/SUS304-900-4hr specimens during the first scan. The G/SUS304-900-4hr exhibits the highest corrosion current indicating that its surface has the worst corrosion resistance among all samples. By contrast, because of the lack of complete graphene protection on the surface, the corrosion current of the G/SUS304-900-4hr differed from the corrosion currents of the other two specimens by an order of magnitude. It demonstrates that this specimen was most vulnerable to corrosion. To simulate the long-term of corrosion under laboratory circumstances, the samples were immersed in the corrosive electrolyte for twenty scans. As Figure 4(b) indicated, the corrosion current for the SUS304 specimen increased from 10^{-7} to 10^{-6} A-cm^{-2}, and the corrosion potential decreased from 0.04 V to -0.24 V after twenty polarization scans. When the voltage was raised between -0.13 V and -0.1 V, a passive film formed on the surface of the stainless steel to prevent the continued dissolution of the inner metal. During upward scanning, pits start growing at the pitting potential (0.38V) in the transpassive region of the polarization curve, where the current increases sharply from the passive current level due to a breakdown of the passive film. As figure S4(a) shows, micropores and rust were clearly observed on the testing area of the SUS304 after prolonged corrosion. However, after twenty polarization-curve scans, the corrosion current for the G/Ni/SUS304-900-4hr specimen remained at relatively low corrosion current (10^{-7} A-cm^{-2}). No passivation or pitting polarization curve similar to the curve of the SUS304 specimen was observed on the G/Ni/SUS304-900-4hr specimen. The complete surface coverage of the graphene coating, as demonstrated in Figure 2(e), effectively prevented the chloride-ion-induced corrosion and slowed the occurrence of passivation.

The optical microscopic images presented in Figure 5 indicate that the surface of the SUS304 was initially bright (Figure 5(a)), with a lined texture attributable to mechanical processing. After 20 polarization tests (Figure 5(b)), large areas of dark brown rust were present on the sample surface (blue arrows); these corroded, rusty regions covered approximately 60% of the tested surface. Several severely corroded regions and numerous sunken holes with diameters of approximately 10~20 µm were also observed (red arrows). In contrast, Figure 5(c) reveals that after the G/Ni/SUS304-900-4hr specimen reacted with methane gas in a high-temperature environment, metal carbides were formed on the surface of the specimen, and the roughness of the surface increased. This finding was consistent with the roughness measurement displayed in Figure S3(d). The optical microscope images show that the dark brown rusty regions and corrosion holes evident on SUS304 (Figure 5(b)) were not observed on the surface of G/Ni/SUS304-900-4hr after polarization testing (Figure 5(d)); even an enlarged view of Figure 5(d) reveals the presence of only a few small, reddish, copper-colored spots of rust on the surface of this specimen (green arrows). Graphene grown via CVD possesses a polycrystalline structure that is naturally deposited at grain boundaries and folds[39, 48, 49]. Thus, the observed results may suggest that the passage of chloride ions through structural defects in the graphene occurred after prolonged electrochemical testing.

Another challenge related to the use of metal bipolar plates in fuel cells is that metals become corroded and oxidized after prolonged exposure to a corrosive environment and the resulting dissolved metal ions tend to poison platinum catalysts, reducing their catalytic capabilities. Fe, Cr, and Ni ions, among other metal ions, will poison such catalysts; in particular, an increase in the iron-ion concentration not only affects the catalytic activities of catalysts but may also cause a dramatic decrease in the conductivity of proton-exchange membranes[50-53]. Figure S4(b) and (c) indicate that after 20 polarization tests, the electrolyte solution for the graphene-protected G/Ni/SUS304-900-4hr stainless steel specimen remained clear; by contrast, because of the release of various metal ions as a result of the oxidation of the specimen structure, the electrolyte solution for the non-graphene-protected SUS304 stainless steel specimen had changed from transparent to a yellowish-brown color. Inductively coupled plasma (ICP) was used

to analyze the types and concentrations of metal ions in the electrolyte solutions. In the SUS304 electrolyte solution, iron, chromium, and nickel metal ions were detected at concentrations of 29 ppm, 6 ppm, and 2 ppm, respectively; however, in the G/Ni/SUS304-900-4hr electrolyte solution, no Fe, Cr, or Ni ions could be detected using an instrument with a lower limit of detection of 0.1 ppm. Therefore, it was evident that the protective graphene layer effectively reduced the concentration of dissolved metal ions released from the stainless steel and thereby slowed the rate of proton-exchange-membrane poisoning.

In addition to corrosion resistance, the low impedance of metal bipolar plates could help to reduce losses in the overall output power of fuel cells. We observed changes in the contact resistances of the SUS304 and G/Ni/SUS304-900-4hr specimens before and after polarization testing. Figure 6(a) indicates that the contact resistance gradually decreased as the compaction force increased. This phenomenon occurred because the number of contact points between the stainless steel coating and the carbon paper increased with increasing compaction force. After corrosion by chloride ions, the contact resistance of the SUS304 specimen increased from 158 m ohm cm^2 to 560 mohm cm^2 (under a compaction force of 140 N cm^{-2}), which corresponds to a 250% increase. As depicted in the anodic polarization curve for SUS304 stainless steel shown in Figure 4, an increase in voltage produced only a small change in current. However, although the metal oxide film that forms on the surface of stainless steel through passivation can slow the corrosion rate, this film also increases the contact resistance, leading to an increase in the internal resistance of the fuel cell and negatively impacting the cell's power-generation efficiency. The graphene barrier on the surface of the G/Ni/SUS304-900-4hr specimen also slowed the rate of oxidative corrosion; thus, no significant passivation was observed in the anodic polarization curve of this specimen. The experiments revealed that the contact resistance of the Ni/SUS304-900-4hr specimen only slightly increased after polarization testing (Figure 6(b)); this resistance increased by only 20% (from 30 mohm cm^2 to 36 mohm cm^2). A graphene coating with complete surface coverage on stainless steel not only provides corrosion protection but also exhibits excellent electrical conductivity.

During fuel-cell operation, hydrogen ions pass through the proton-exchange

membrane to react with oxygen at the cathode to form water. Prolonged fuel-cell use will generate acid anions, such as SO_3^-, SO_4^-, HSO_4^-, and F^-, in the polymer electrolyte membrane. If the contact angle between the material of the bipolar plate and the water is small, the generated water can readily accumulate in the channels of the bipolar plate; this phenomenon may lead to the blocking of these channels and can create an acidic environment that accelerates the corrosion of the bipolar plate, degrading fuel-cell performance. Proper drainage can also help to accelerate the dissipation of heat produced when a fuel cell generates power. Therefore, with respect to fuel-cell performance, the hydrophobicity of the bipolar plates is a critical issue that must be addressed. Because of its non-polar covalent-bond structure, graphene exhibits hydrophobic characteristics that prevent it from engaging in hydrogen bonding with water molecules[54]. As indicated in Figure 6(c) and Figure 6(d), contact angle measurements revealed that the presence of a graphene coating increased the angle at which water contacted the stainless steel from 65° to 101°, significantly increasing the hydrophobicity of the stainless steel.

2.2 Tuning the layers of graphene on stainless steel substrate by using a buffering layer atop stainless steel.

In this section, we further explored the graphene growing mechanism in different thickness of Ni and $TiSi_2$ layer on stainless steel. Nickel metal is an excellent catalyst for the growth of graphene. Conversely, $TiSi_2$ layer is not catalytic to decompose carbon gases. Figure 7 (a, c, e) were raman I_{2D}/I_G mapping of 40,80,160 nm of nickel / stainless steel, respectively. The value of I_{2D}/I_G are from 0.3 to 1.5 indicate that a few layers graphene structure grown on the substrate. Figure 9 (a, c, e) SEM clearly showed that graphene layers coated on the surface of Ni/SS. The dissolution of carbon into nickle bulk and the subsequent non-equilibrium precipitation lead to the non-uniformity CVD graphene. As the statistics result showed in table S2, the smaller standard deviation value of I_{2D}/I_G ratio means the more uniformity graphene are achieved. Shown in fig. 8(a,b) are the D/G intensity ratio of graphene film and the grain size plotted as a function of the metal thickness. As fig.8 (a) showed, I_D/I_G value of 40 nm Ni/SS, 80nm Ni/SS, 160nm Ni/SS were 0.71, 0.56, 0.27, thickness of nickel influence the quality of graphene formed on top. While thickness of nickel layer increasing, the graphene's I_D/I_G defect signals

become weaker. During the CVD process, several metal element in stainless steel will diffuse into nickel bulk. Nickel layers not only be a catalyst to decompose carbon gas, but also act as a barrier to reduce the other metal element reach the nickel surface. A variety of catalyst react with methane at the same time will cause the poor quality graphene, the thicker nickel layer could mitigate this negative effect from the substrate of stainless steel. The better quality and bigger grain size graphene are grown on 160 nm Ni/SS than on 40nm and 80nm Ni/SS substrate. As fig. 7(b) showed, the ratio of I_D/I_G of 40 nm $TiSi_2$/SS, 80nm $TiSi_2$/SS, 160nm $TiSi_2$/SS are 0.88, 1.76, 2.67, respectively.While thickness of $TiSi_2$ layer increases, the defect of growing graphene also significantly increased. Not like a carbon-dissloving nickel layer, $TiSi_2$ is a carbon-rejection layer, preventing carbon atoms decomposed from carbon source diffuse into to stainless steel during CVD process. It is noticed a amorphous carbon raman spectrum[55],with a broad D peak and G peak positon at 1606 cm^{-1}, appear on 40nm $TiSi_2$ / SS, 80nm $TiSi_2$/SS, 160nm $TiSi_2$/SS substrate react with methane gas for 60mins. While reaction time was extended to 180 mins, only 40nm $TiSi_2$/SS showed characteristic signals of the graphene, having a strong G peak(around at 1584 cm^{-1}) peak and 2D peak. But 80nm $TiSi_2$/SS and 160nm $TiSi_2$/SS still show the amorphous carbon raman signal. This result is coincide with the fig.9(b, d, f) SEM images. Highly-crystallized graphene layers are clearly to see on the surface(fig. 9b), however, the graphene sheet is not easy to found on 80nm $TiSi_2$/SS-180 mins and 160nm $TiSi_2$/SS(fig. 9d, f). We suggest the Cr, Fe, Ni atoms in stainless steel will diffuse into $TiSi_2$ layer during CVD process . Too thick $TiSi_2$ layer will cause those elements not to reach surface. Without catalytic metal on the top of $TiSi_2$ layer, it s difficult to grow high quality graphene. A surprising result was found at table S2, standard deviation of I_{2D}/I_G ratio of $TiSi_2$/SS is 0.04 to 0.11, smaller than I_{2D}/I_G standard deviation values, 0.15 to 0.2, of Ni/SS. That indicates that carbon-rejection $TiSi_2$ layer can assist to grow more uniform graphene than carbon-dissloving Ni layer.

As figure 9 (a-f) SEM showed, after Ni/SS and $TiSi_2$/SS react with methane gas with long time, there is seem some new compound deposited on graphene layer. In images of the actual specimens, the surface of the 40nm Ni/SS(Figure S5(a)) and 40nm $TiSi_2$/SS(Figure S5(d)) appeared gray and black, respectively.While the methane flow

rate was increased from 0.3 sccm to 1.0 sccm, surface of the 40nm Ni/SS-120mins and TiSi$_2$/SS-120mins (fig.S6 (g, k)) both transfer black to silver. The 40nm TiSi$_2$/SS-90 mins specimen (Fig.S6 (f)) show the transition condition, about 50% of the area has been gradually covered by silvery white upper material. The red dashed line at Figure 10(a) indicate the black-silver area boundary. Figure 10(b) provides the direct evidence that graphene layers are gradually covered with silver layer (as blue arrow point). Same phenomena also occur at 40nm Ni/SS subatrate , as figure 10(d) show that the atop layer almost cap over the graphene film(as blue arrow point). We suggest the transition of the growing process will happen with a longer reaction time. Figure 11 raman spectrum show another proof for this phenomenon. As the figure 11 show that the black area of 40 nm TiSi$_2$/SS-90mins sample where the graphene is exposed appear the graphene distinctive signal. Nevertheless, the silver area where graphene was coverd do not show carbon signal. Raman detection result is consistent with the Fig.10 SEM images. Diffusion profile were qualitatively studied using EDS by line scanning mode. These results are shown in Fig. S7 (a,b) and Table S3. As the Fig S7(a) show, the three main elements on the surface of TiSi$_2$/SS are Cr, Fe, C atoms. Table S3. shows the EDS composition of element on (A)stainless steel bulk, (B) the interface between stainless steel and top layer, (C) the surface of top layer. Detecting position are marked as fig.S7(b) showed. It was found that the Cr and Fe atoms out-diffusion from stainless steel bulk to surface(A to C). Conversely, carbon atoms in-diffusion into stainless steel bulk. We suggest that iron diffuse out to the surface, assist the carbon gas decompose. The enriched level of carbon on surface start to drive graphene nucleation . Later, the more and more out-diffusion Cr and Fe atoms capture higher carbon concentration to form chromium iron carbides layers which gradually cap over the graphene layers.

Since in 2.1 section, 100% complete coverage graphene are grown on 5um Ni/SS effectively improve the corrosion resistance of stainless steel. We expect the chromium iron carbides/graphene double barrier could further boost the resistance performance of stainless steel. Figure 12 (a) shows the polarization curves of the tenth scan. The corrosion current (I corr.) of the bare 40nm TiSi$_2$/SS polarization and bare 40 nm Ni/SS was 1.45×10^{-7}, 3.23×10^{-6} A-cm^{-2},respectively. As fig.7(a, b) Raman mapping indicated

the 40nm TiSi$_2$/SS-180 mins and 40 nm Ni/SS-180 mins are coated by few layers graphene. After 10 cycles polarization scans, corrosion current of these samples both increased to 10^{-5} order. In addition, the 40nm TiSi$_2$/SS-240 mins, 40 nm Ni/SS-240 mins specimens are covered by metal-carbide/graphenen double layers, display the corrosion current 1.65 x 10^{-5} and 8.15 x 10^{-5}, respectively. All samples perform the worst corrosion resistance after CVD process, even with graphene protecting layers. As red arrows indicate in Fig S7(c-h), several small pores are randomly scattered on all the samples after heating treatment lead to the poor corrosion resistance. In the further, the top layers on stainless steel should be try to keep smooth without pores after CVD process, like fig.2 (f) show. In that way, metal-carbide/graphenen double layers could completely protect the beneath stainless steel substrate.

3. Conclusion

In summary, we demonstrate that an optimal CVD process can be used to synthesize a continuous and high-quality graphene thin film on nickel-buffered stainless steel. The nickel barrier on steel is able to both reduce the formation of metal carbide and catalyze graphene precipitation at high temperatures. Thus it successfully solves the poor graphitization issue on bare SUS304 with no buffer layer. Compared with steels without protection, the graphene-coated steel exhibits outstanding anti-corrosion properties, indicating that the multilayered graphene can effectively prohibit the access of chloride ions into the steel surfaces. The graphene coating on steel also maintains good conductivity and increases its hydrophobicity. It is believed that these environmentally friendly graphene-based steel coatings have the potential to replace chrome and other potentially toxic chemicals. In addition, the more uniform of growing graphene layers could be easily achieved by adjusting the thickness of Ni or TiSi$_2$ layer on stainless steel.

4. Experimental Section
Preparation of the specimen:

A nickel layer of 5 µm in thickness was electroplated onto a 4 x 4 cm^2 SUS304 stainless steel plate with a thickness of 0.5 mm. The specimen was placed in a quartz tube and argon gas (100 sccm) and hydrogen gas (50 sccm) were inlet into this tube. Over 30

minutes of heating, the temperature was increased from room temperature to a predetermined target temperature (700, 800, or 900°C). When this target temperature was reached, methane gas (25 sccm) was inlet into the quartz tube. After the reaction was complete, only the input of the methane gas was terminated; the flow of the argon/hydrogen gas mixture into the quartz tube was continued until the tube had cooled to room temperature.

Raman spectroscopy:

Raman spectroscopy was performed with a Renishaw inVia Raman microscope, using a laser excitation wavelength of 514.5 nm, laser power of 12 mW, scan range of 1,000-3,000 cm^{-1}, 10 s scan time per spot. The size of the focal spot of the laser was 1 µm.

Electrochemical tests:

Polarization testing was carried out with an Autolab PGSTAT30 potentiostat equipped with a frequency response analyzer. Ag/AgCl was used as the reference electrode, and Pt was used as the counter electrode. The standard reduction potential corresponding to the standard hydrogen electrode (SHE) was 0.199 V. The working electrode (WE) was connected to the specimen. Polarization-curve measurements were performed in a 3.5 wt% NaCl solution at ambient temperature. The tested area was 1.76 cm^{2} and the scan rate was 5 mV/s.

Interfacial contact resistance measurement(ICR):

The setup consisted of a hydraulic press with a load capacity of 25 kN, a load sensor with a measurement range of 0–25 kN and an accuracy of 0.1%, a micro-ohmmeter with a resolution of 0.1μΩ. The experimental setup was used to obtain the constitutive relation between the contact resistance and pressure. The stainless steel was sandwiched between two flat carbon paper of the same material and processing conditions as the bipolar plate. The sandwiched carbon papers /stainless steel assembly was then placed between two copper plates. The range of the operating load was 0-196 $N·cm^{-2}$ for recording ICR values at every 9.8 $N·cm^{-2}$.

X-ray diffraction:

X-ray diffraction patterns were obtained with a Bruker D2 Phaser (copper target, characteristic wavelength: 1.54 Å), using a voltage of 30 kV, a current of 20 mA, a scan

rate of 1° every 6 seconds, and a scan range of 20-90°.

Surface roughness measurement:

Surface roughness was measured using a Chroma 7502 white-light interferometer (WLI), with a vertical resolution of 0.1 nm and horizontal resolution of 0.5 µm.
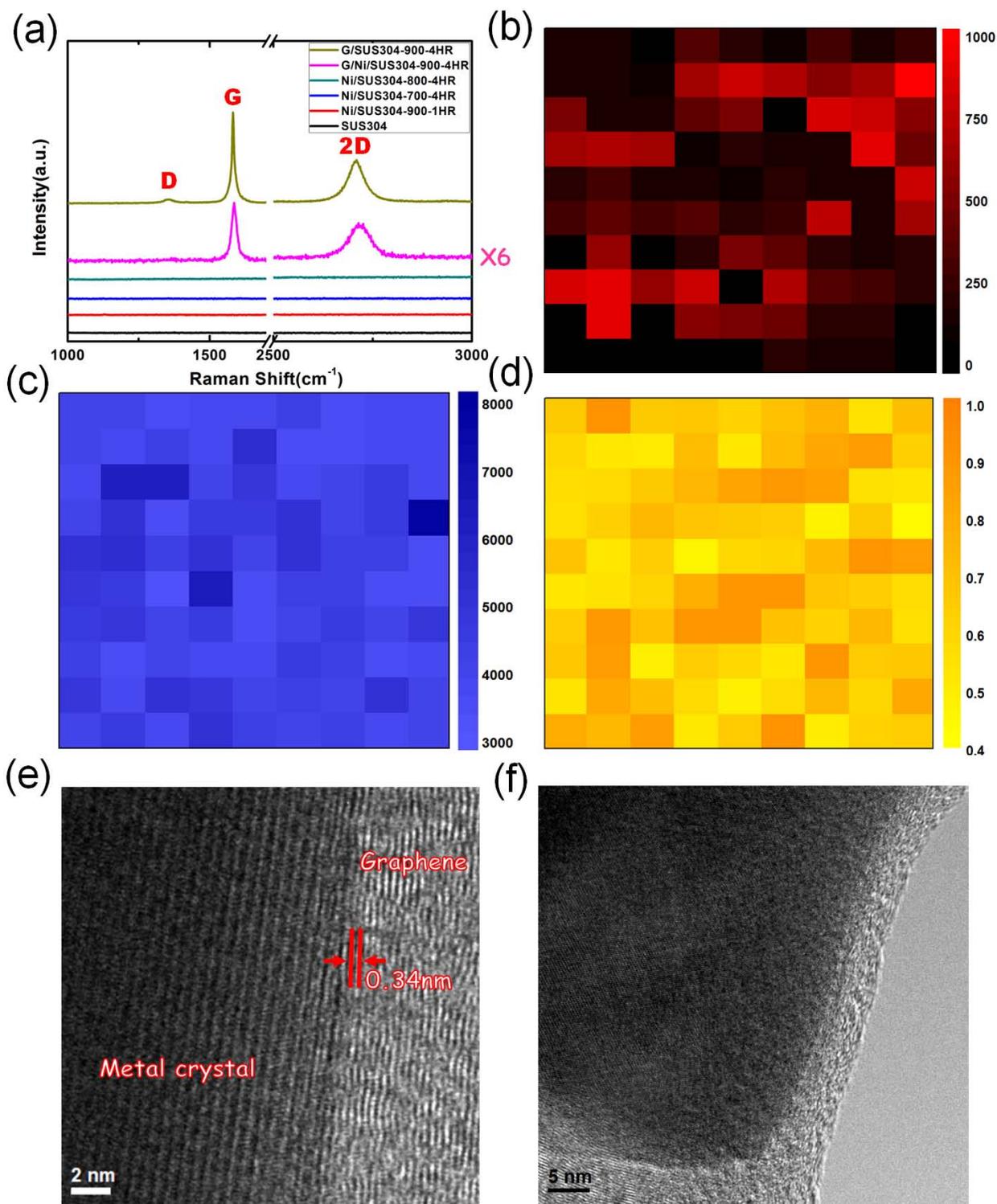
Figure 1. (a) Raman spectra; (b,c) G Raman peak mapping of G/SUS304-900-4hr and G/Ni/SUS304-900-4hr, respectively; (d) I_{2D}/I_G Raman peak mapping of G/Ni/SUS304-900-4hr; (e,f) cross-sectional TEM image of G/Ni/SUS304-900-4hr
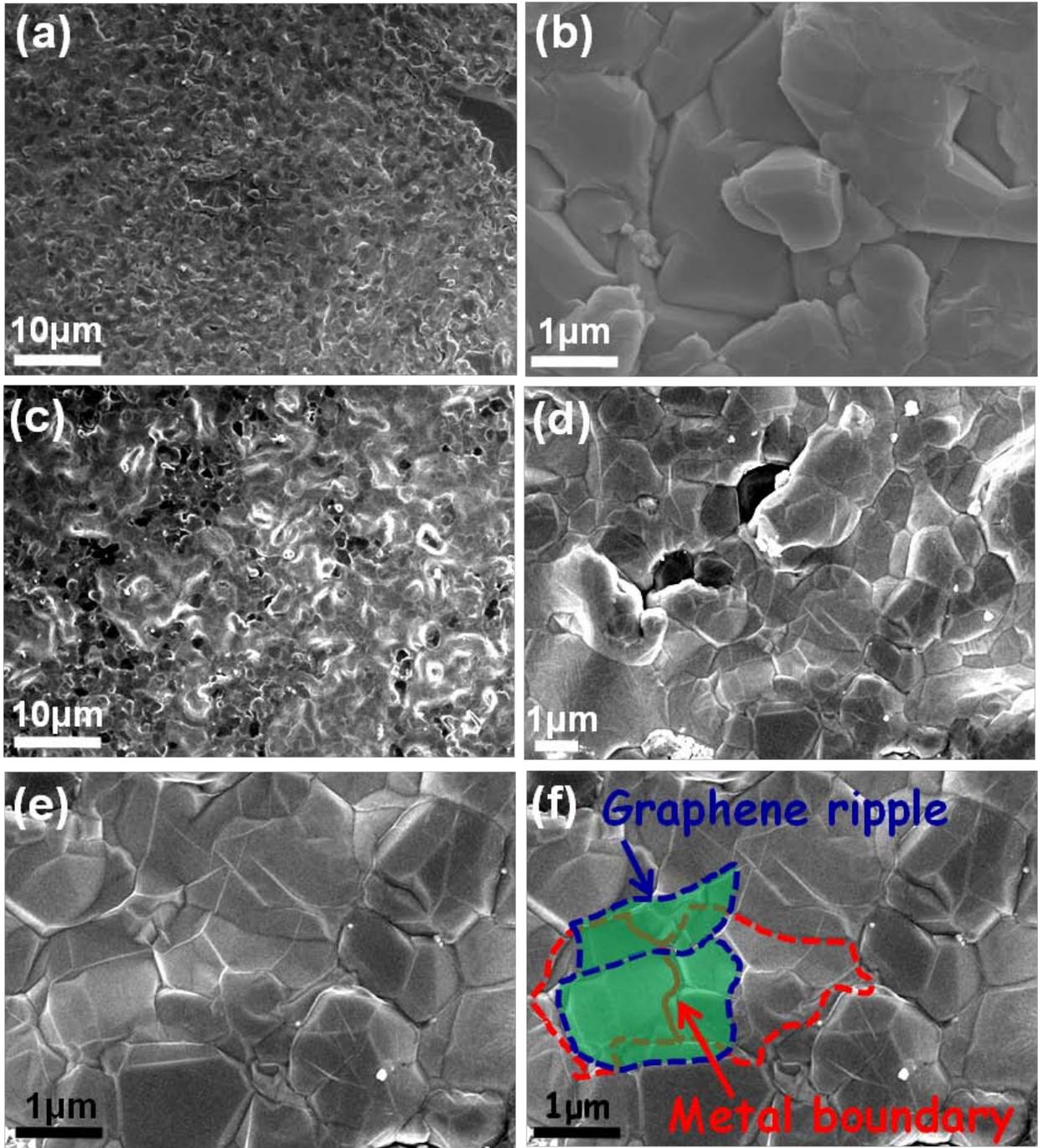
Figure 2. SEM images at (a, b) 2,000X and 20,000X magnification of G/SUS304-900-4hr, respectively; (c, d, e) 2,000X, 10,000X, 20,000X magnification of G/Ni/SUS304-900-4hr, respectively; (f) the red line outlines the metal grain boundary, the blue line outlines the graphene ripples, and the green area shows the metal boundaries covered with a graphene film
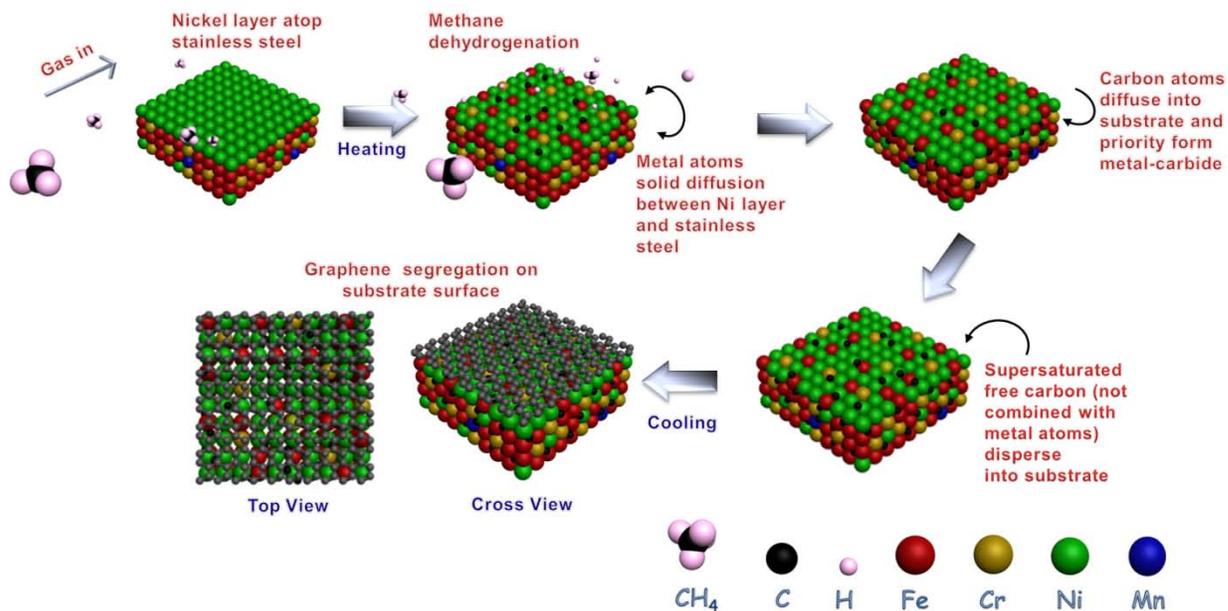
Figure 3. Schematic diagram of the graphene formation mechanism on Ni/SUS304 substrate
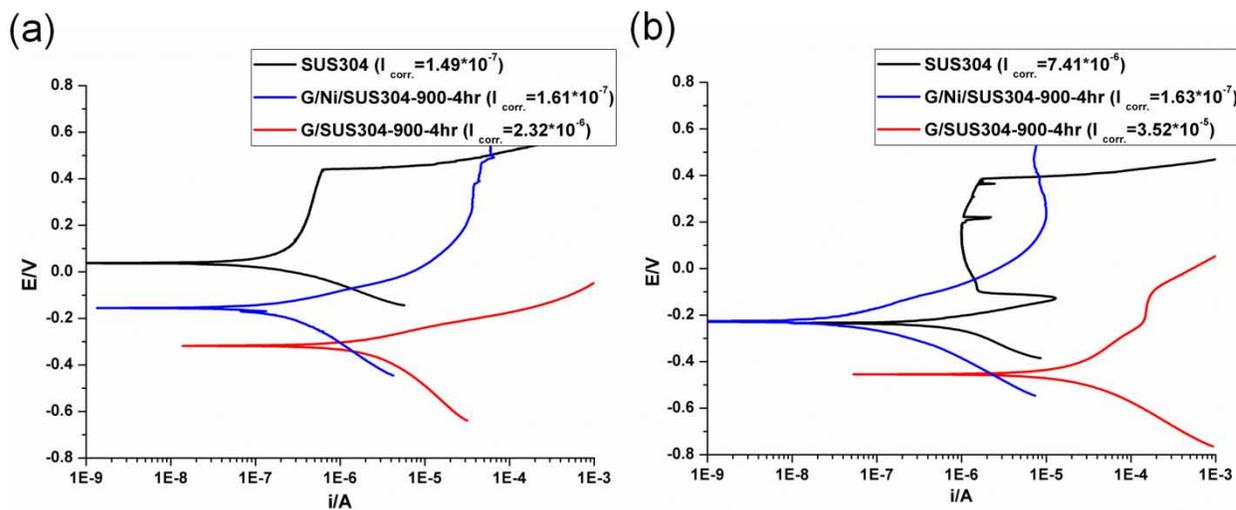
Figure 4. Tafel plots of SUS304 (black line), G/SUS304-900-4hr (red line), G/Ni/SUS304-900-4hr (blue line) for the (a) first scan and (b) twentieth scan
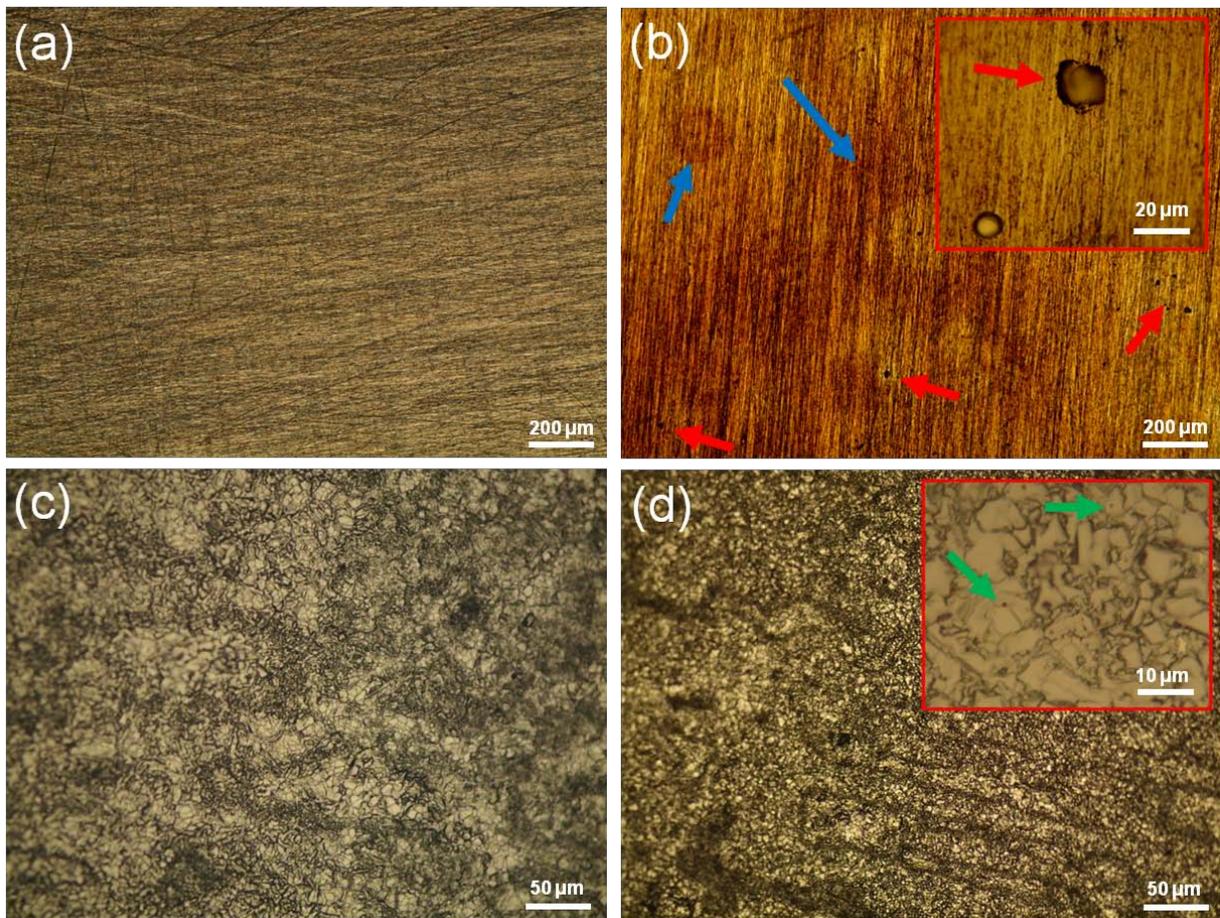
Figure 5. Optical microscopy images of (a) SUS304, (b) SUS304 after polarization (inset: a local enlarged view), (c) G/Ni/SUS304-900-4hr, (d) G/Ni/SUS304-900-4hr after polarization (inset: a local enlarged view)
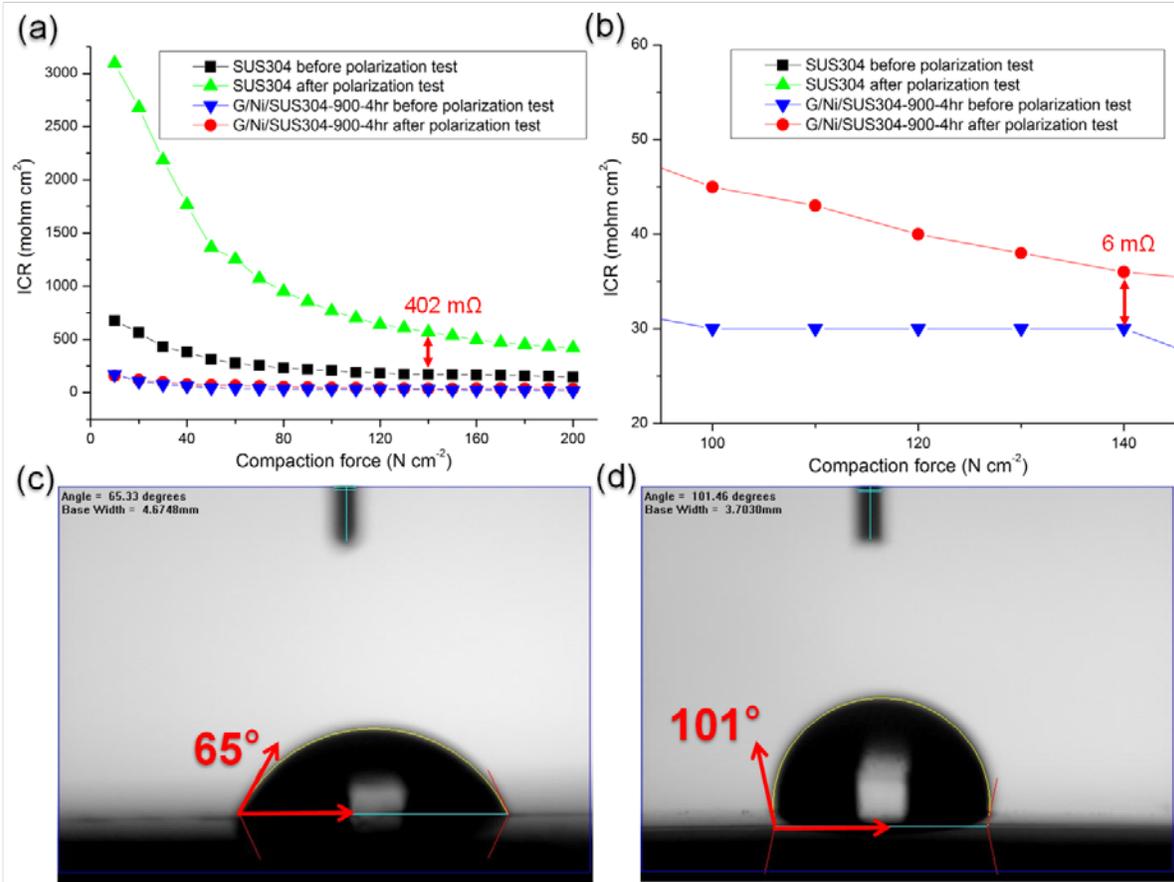
Figure 6. (a) Plot of interfacial contact resistance against compaction force; (b) an enlarged view of the contact resistance plot (focused on a compaction force of 140 N cm^{-2}); (c,d) water contact angle on SUS304 and G/Ni/SUS304-900-4hr specimens, respectively.
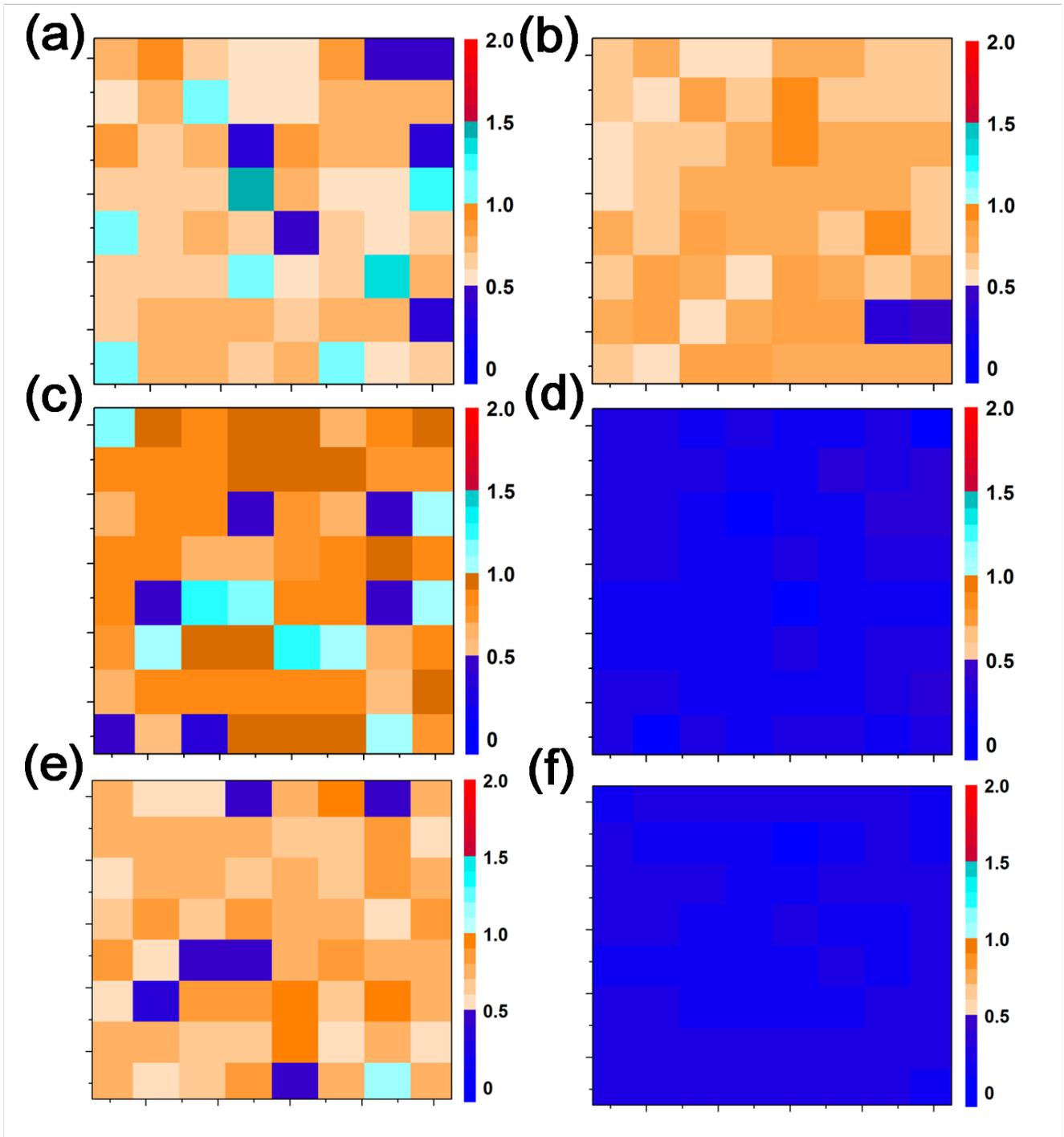
Figure 7. I_{2D}/I_G Raman peak mapping of (a, c, e) 40nm Ni/SS-180 mins, 80nm Ni/SS-180 mins, 160nm Ni/SS-180 mins, (b, d, f) 40nm TiSi$_2$/SS-180 mins, 80nm TiSi$_2$/SS-180 mins, 160nm TiSi$_2$/SS-180 mins.
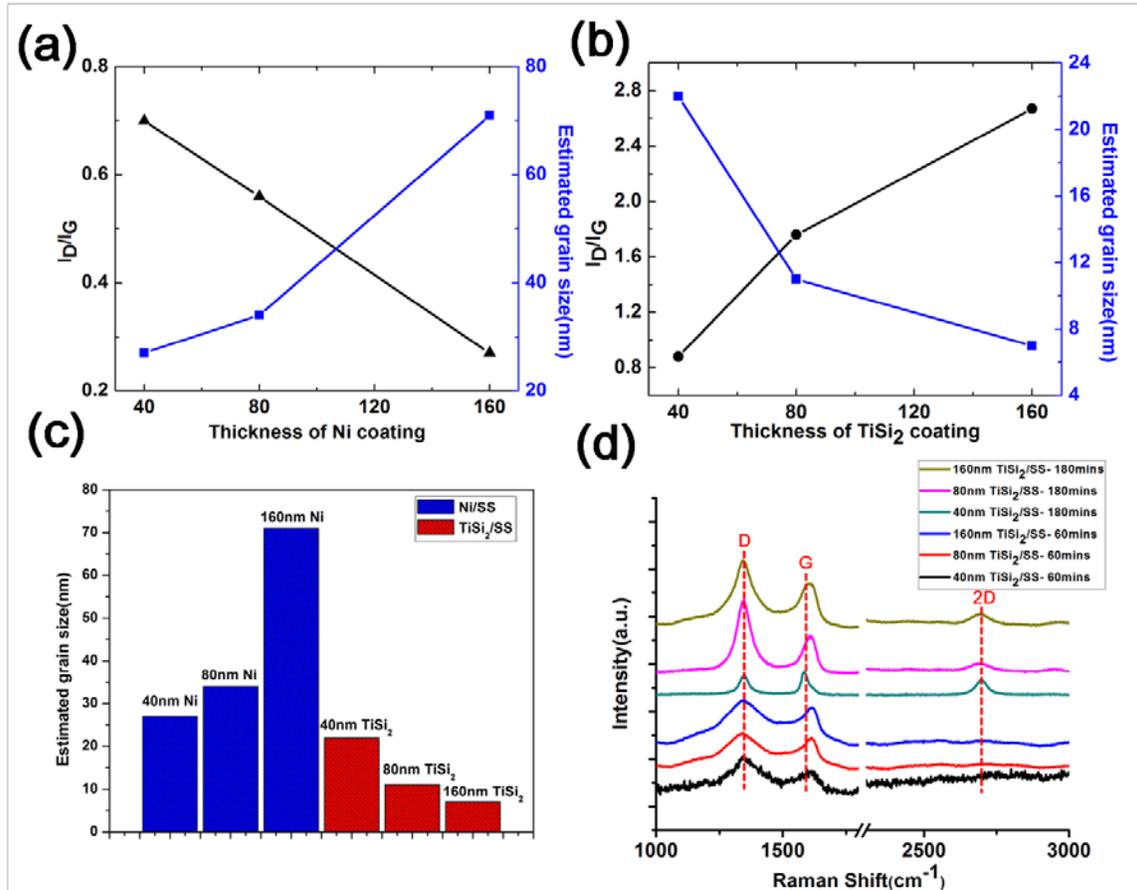
Figure 8. (a,b) Estimated grain size of graphene based on D/G peak intensity ratio of Ni/SS and TiSi$_2$/SS, respectively. (c)Histogram of estimated grain size (d) Raman spectra of TiSi$_2$/SS substrate.
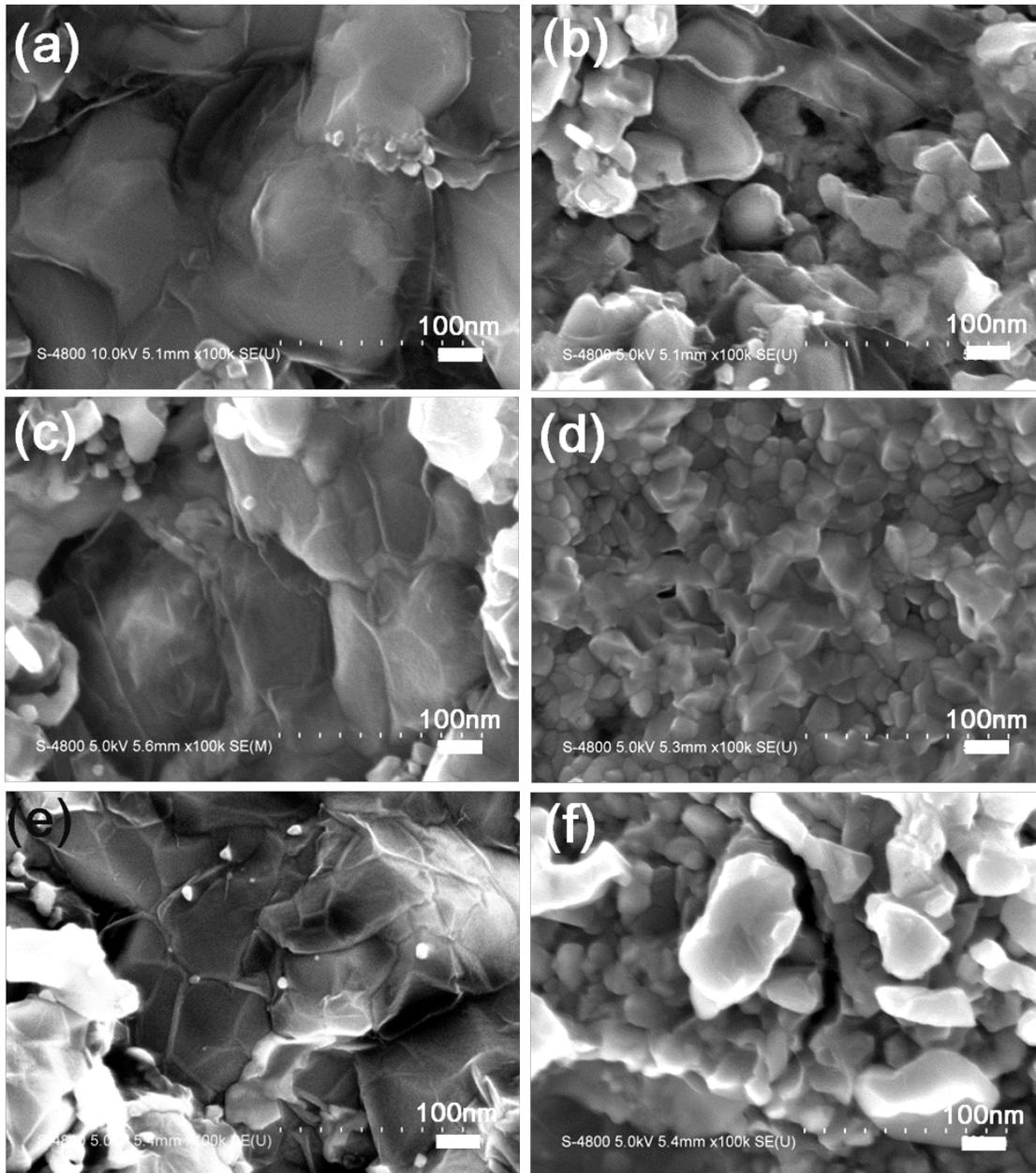
Figure 9. SEM images at (a, c, e) 40nm Ni/SS, 80nm Ni/SS, 160nm Ni/SS react with 0.3 sccm methane gas flow of for 180 mins,respectively. (b, d, f) 40nm $TiSi_2$/SS, 80nm $TiSi_2$/SS, 160nm $TiSi_2$/SS react with 0.3 sccm methane for 180 mins, respectively.
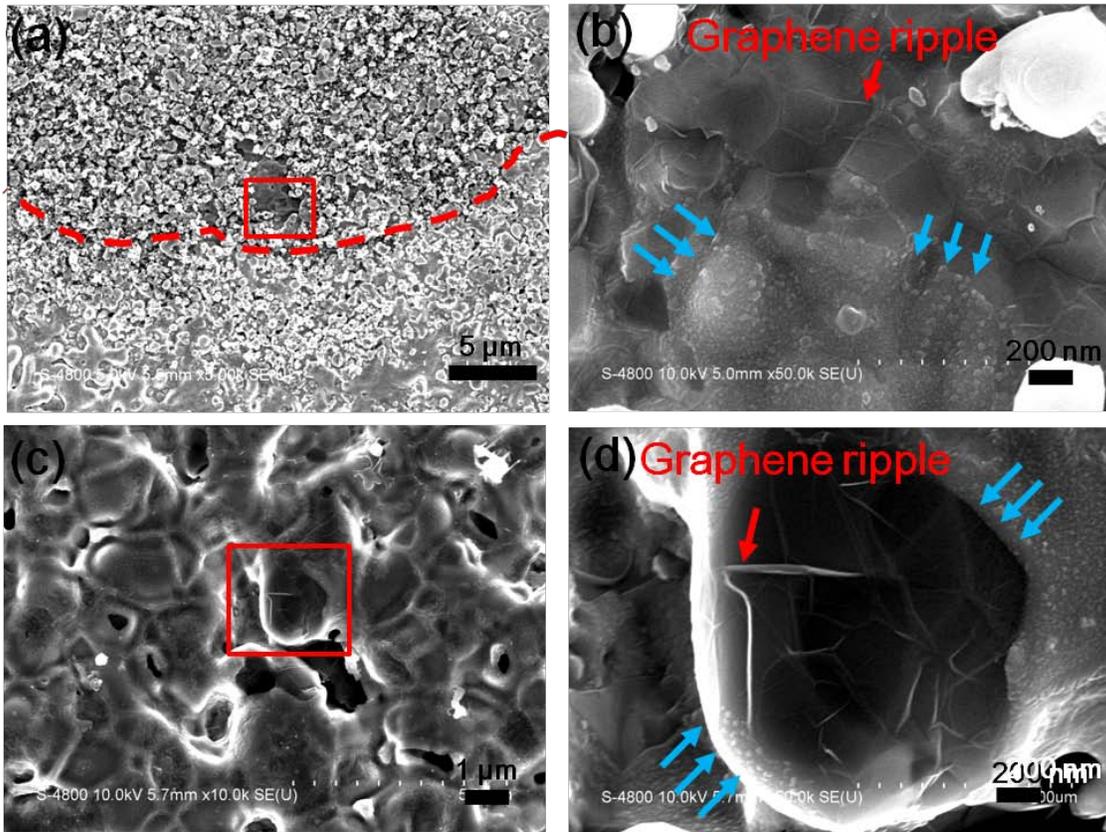
Figure 10. SEM images (a)transition area of the 40nm TiSi/SS-90mins substrate (dash line indicate the transistion boundary), (b)enlarged view of square area of (a), (c)40nm Ni/SS-240mins substrate, (d) enlarged view of square area of (c).(blues arrows at (b, d) show graphene layers were gradually coverd).
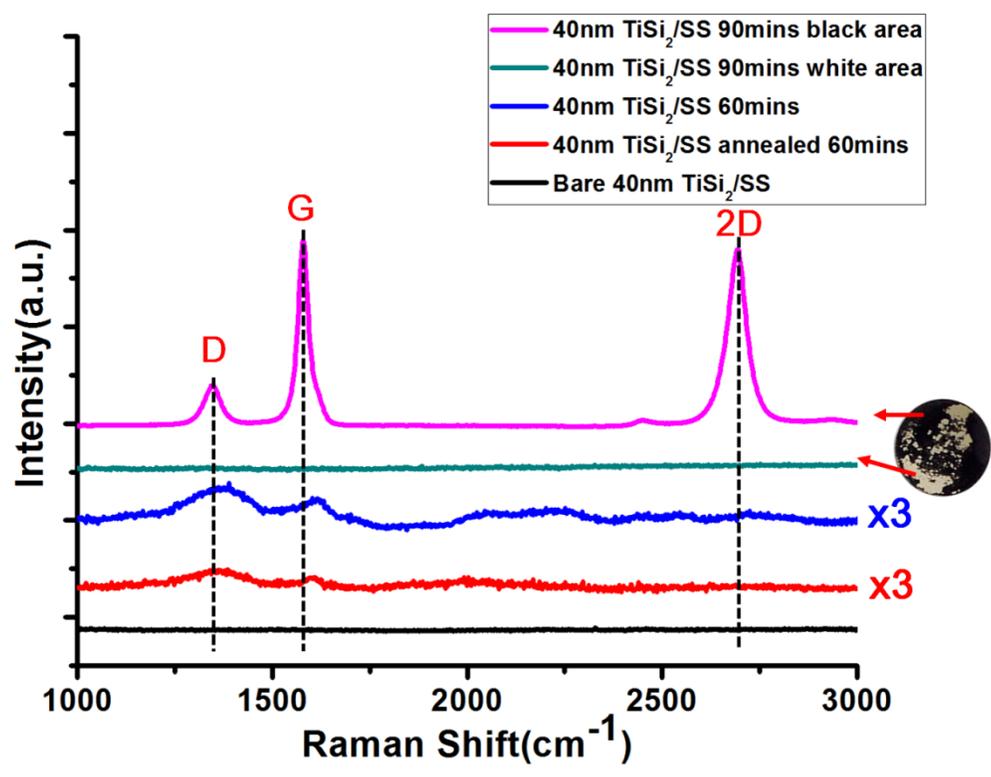
**Figure 11.** Raman spectrum of 40nm TiSi/SS with different CVD reation time.
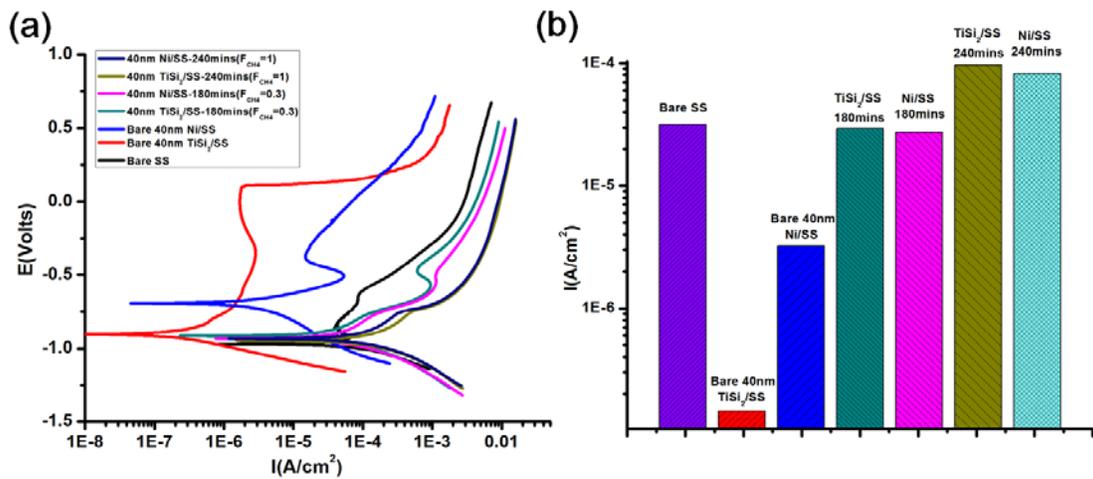
Figure 12. (a) Tafel plots of bare SS, bare 40nm TiSi/SS, bare 40nm Ni/SS, 40nm TiSi$_2$/SS-180mins, 40nm Ni/SS-180mins, 40nm TiSi$_2$/SS-240mins, 40nm Ni/SS-240mins for the tenth scan ,(b)Histogram of corrosion current.

Supporting Information

Table S1. Chemical composition (wt%) of SUS304

Elements	C	Mn	Si	P	S	Cr	Ni	Fe
wt(%)	≤ 0.07	≤ 2.00	≤ 1.00	≤ 0.035	≤ 0.030	17.00~19.00	8.00~11.00	balance

Table S2. Average and standard deviation of I_{2D}/I_G of Ni/SS and TiSi$_2$/SS substrate.

Sample	40 nm Ni/SS	80 nm Ni/SS	160 nm Ni/SS	40 nm TiSi$_2$/SS	80 nm TiSi$_2$/SS	160 nm TiSi$_2$/SS
Average	0.71	0.83	0.71	0.71	0.21	0.20
Standard deviation	0.2	0.18	0.15	0.11	0.07	0.04

Table S3. EDS composition depth profile of elements on 40nm Ni/SS-90mins substrate

| Element	A	B	C
C	N/A	76.58	90.07
Cr	20.24	7.28	3.11
Fe	71.77	15.86	6.71
Ni	6.96	0.28	0.11
Si	1.04	N/A	N/A
Totals	100.00	100.00	100.00
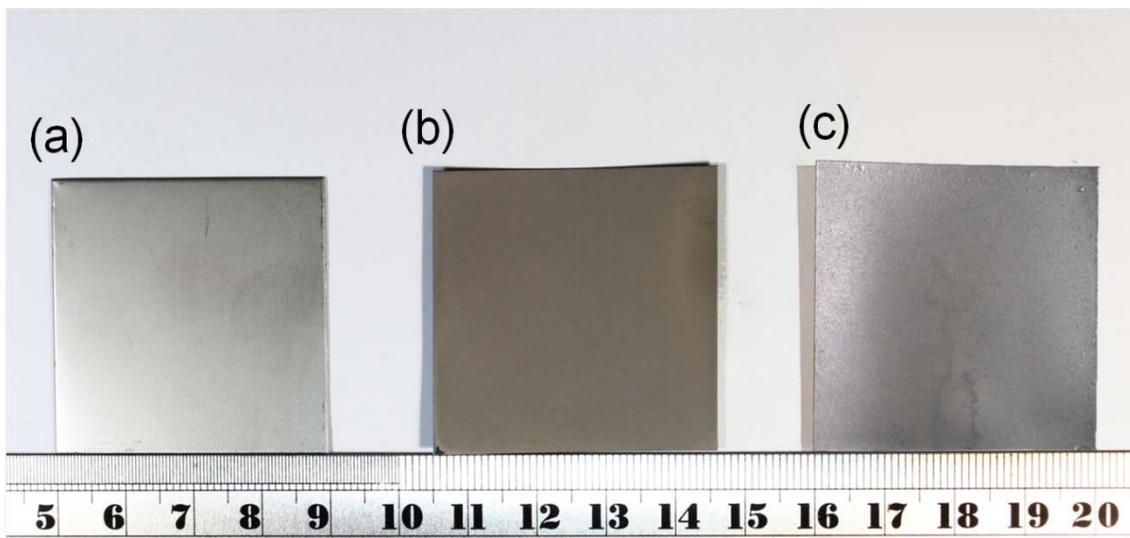
Fig. S1. Photos of (a) SUS304, (b) G/SUS304-900-4hr, and (c) G/Ni/SUS304-900-4hr.
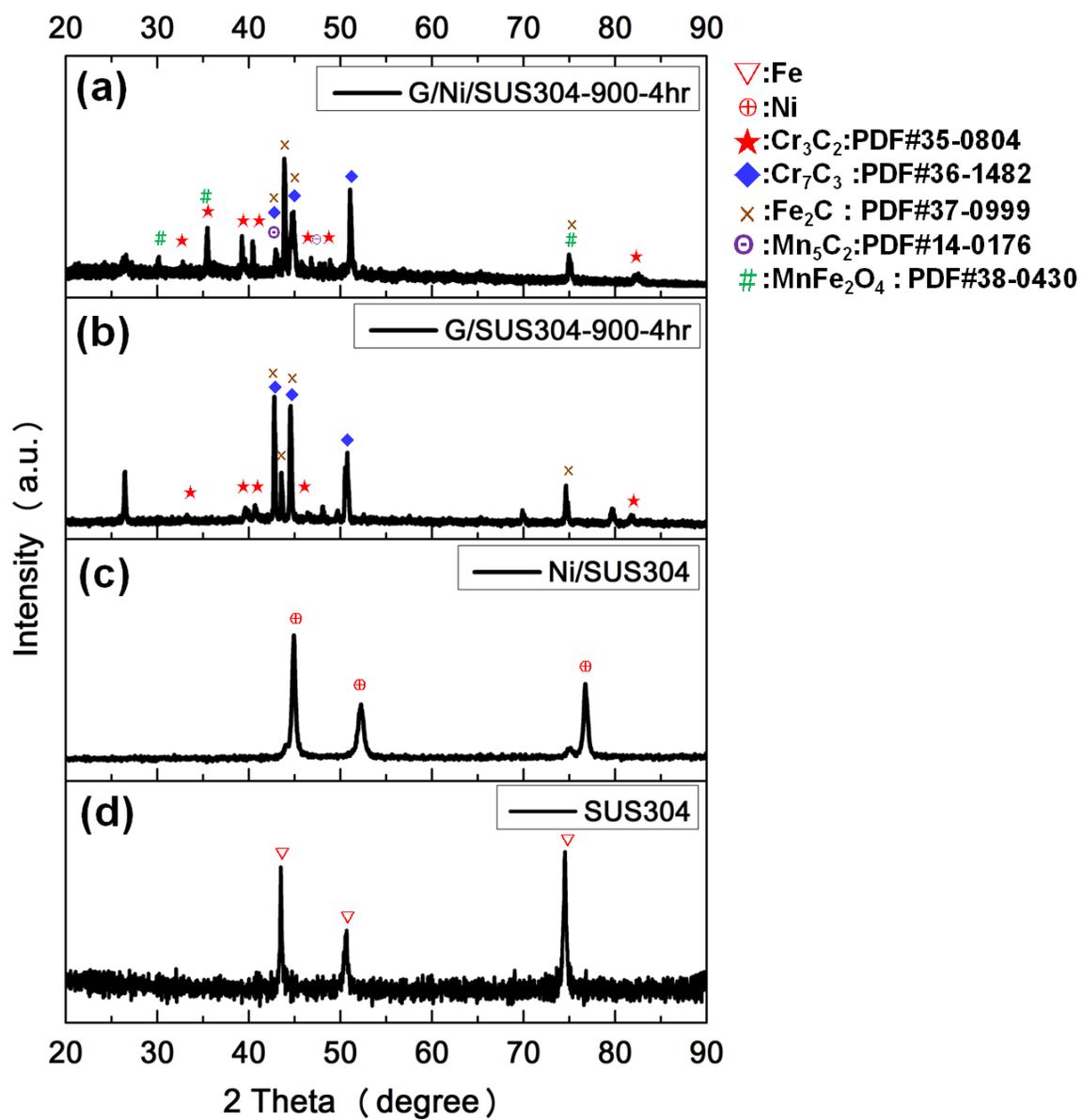
**Fig. S2.** XRD patterns of (a) G/Ni/SUS304-900-4hr, (b) G/SUS304-900-4hr, (c) Ni/SUS304, and (d) SUS304.
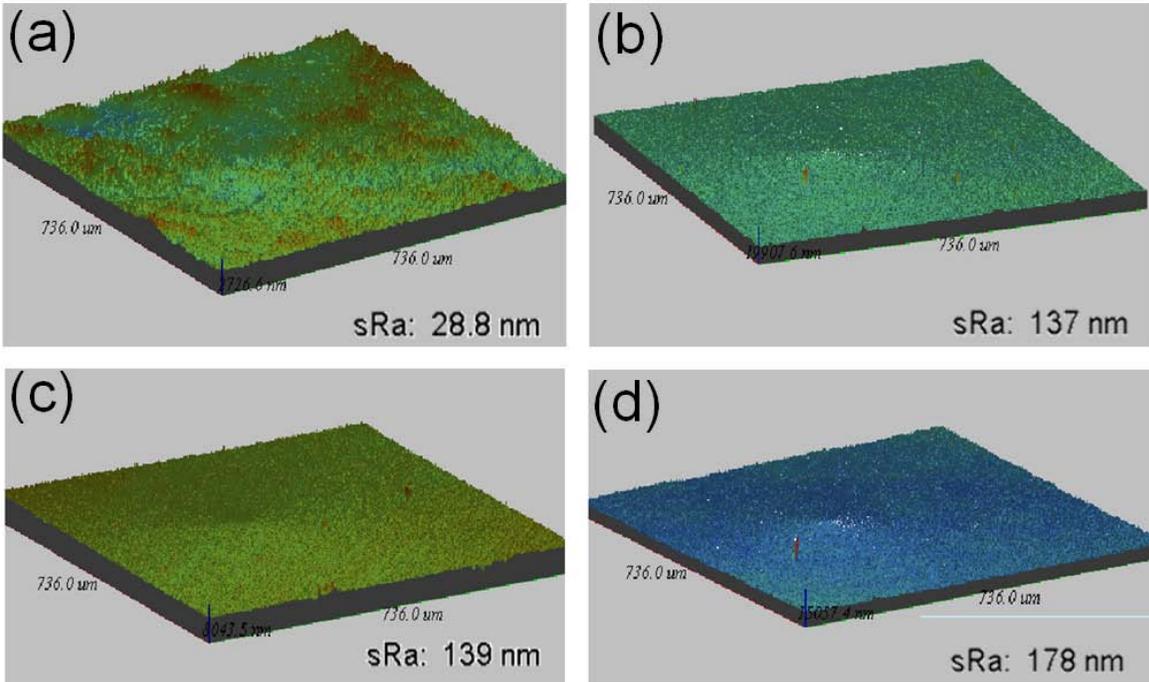
Fig. S3. Surface roughness measured by WLI of (a) SUS304, (b) G/SUS304-900-4hr, (c) Ni/SUS304, and (d) G/Ni/SUS304-900-4hr.
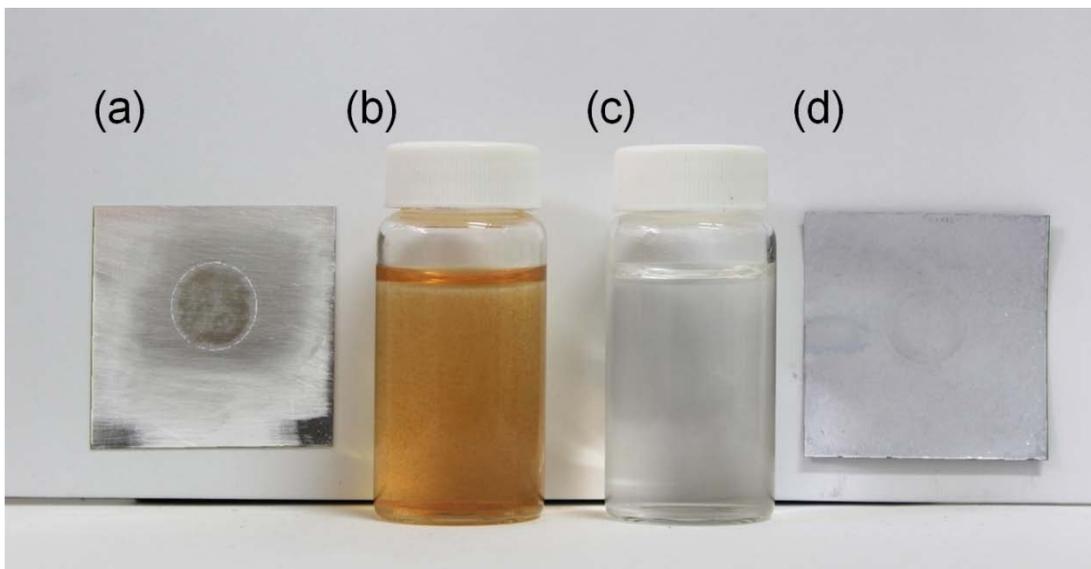
Fig. S4. Photos of samples after 20-cycle polarization test, (a) SUS304 , (b) electrolyte of SUS304 , (c) electrolyte of G/Ni/SUS304-900-4hr, and (d) G/Ni/SUS304-900-4hr.
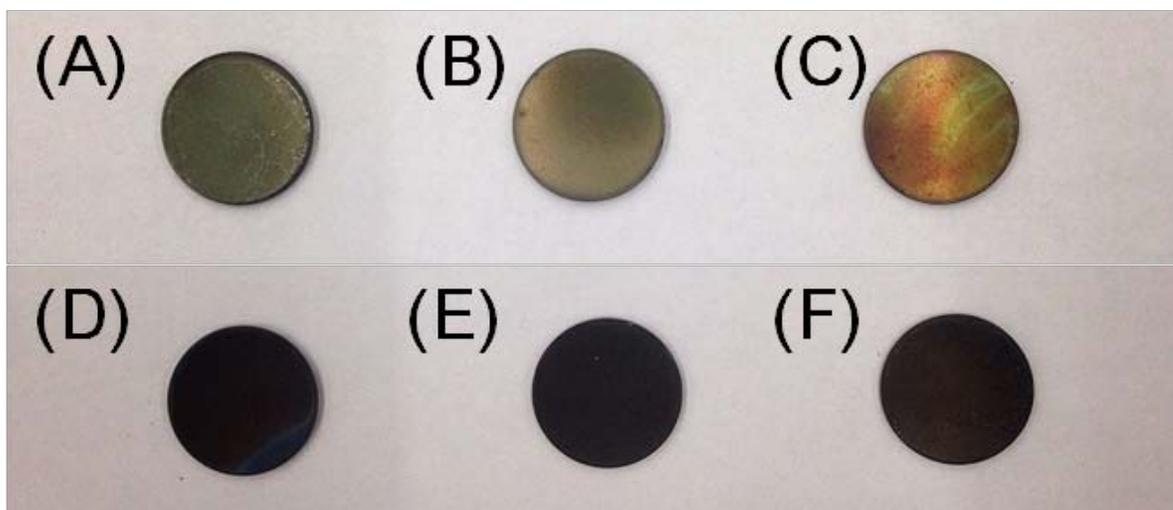

Fig. S5. Photos of (a, b, c) 40nm $TiSi_2$/SS react with 0.3 sccm methane gas for 60 mins, 90 mins, 120 mins, 240 mins, respectively. (d, e, f) 40nm Ni/SS react with 0.3 sccm methane gas for 60 mins, 90 mins, 120 mins, 240 mins, respectively.
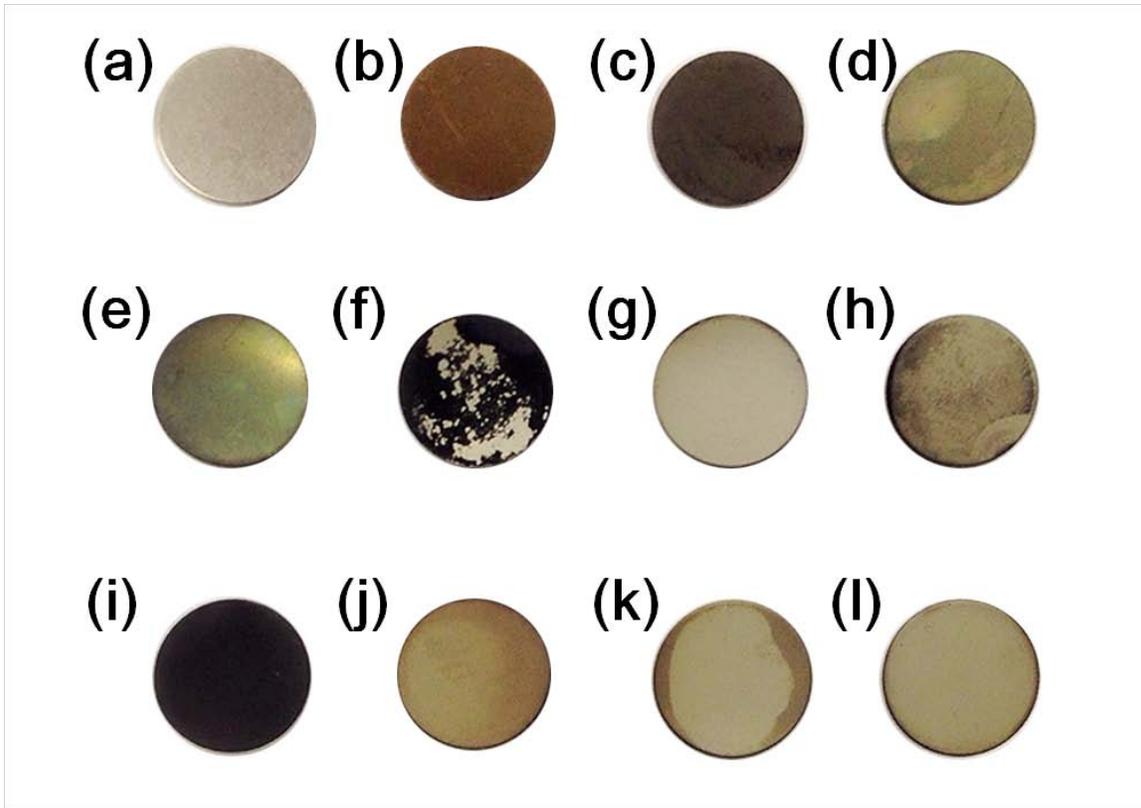
Fig.S6. Photos of (a) Stainless Steel(SS), (b-d) 40nmTiSi$_2$/SS, 40nmNi/SS and SS annealed for 60mins(without methane), (e-h) 40nm TiSi$_2$/SS substrate react with 1.0 sccm methane gas for 60 mins, 90 mins, 120 mins, 240 mins, respectively. (i-l) 40nm Ni/SS substrate react with 1.0 sccm methane gas for 60 mins, 90 mins, 120 mins, 240 mins, respectively.
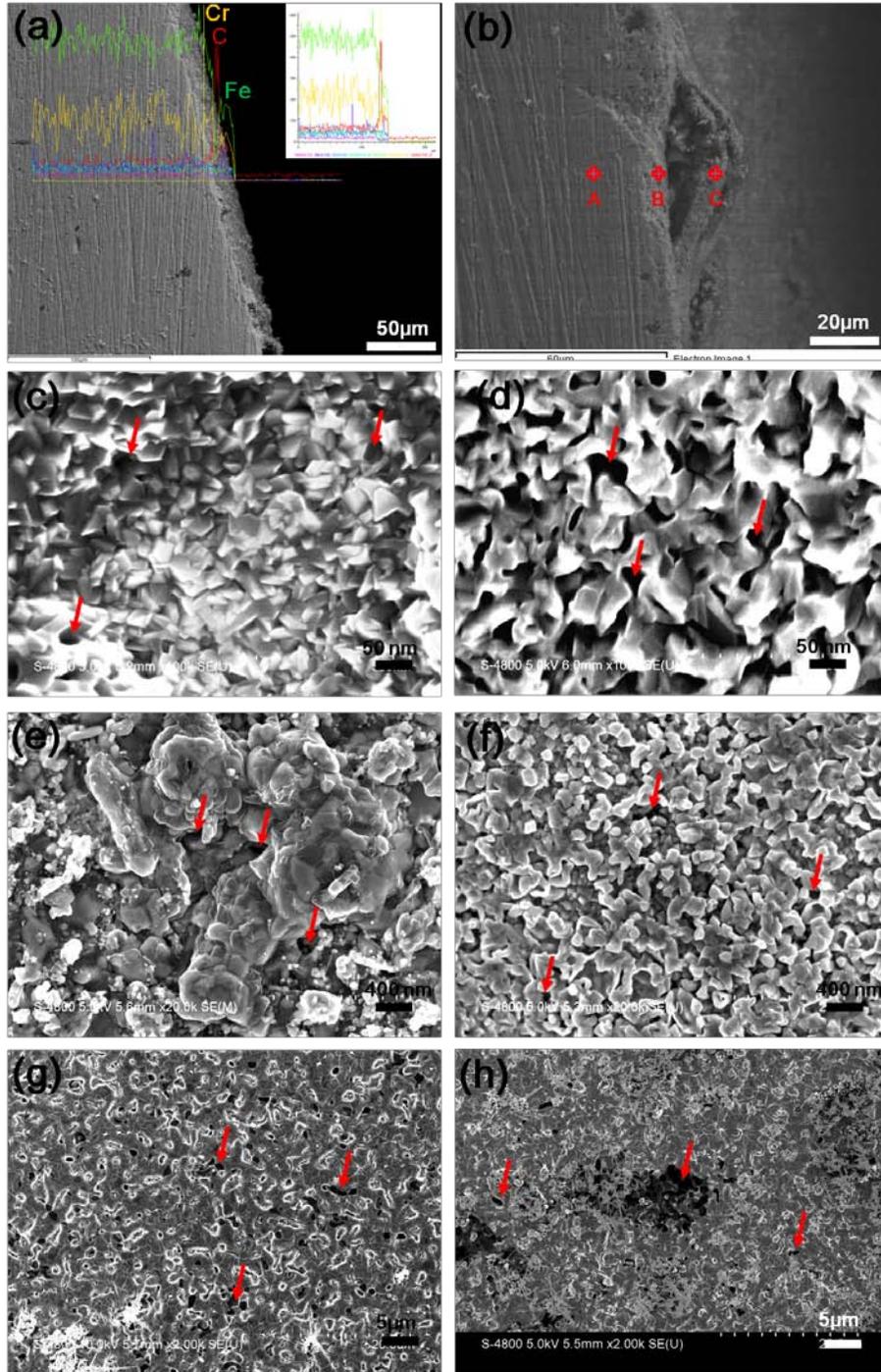
Fig. S7.SEM images at (a) EDS composition depth profile of elements, (b) EDS composition analysis on 40 nm TiSi/SS-240 mins substrate(spotA: stainless steel bulk, spotB: the interface between stainless steel and top layer, spotC: the surface of top layer, (c,d) 80nm Ni/SS, 80 nm TiSi$_2$/SS annealed for 180 mins(without methane), (e,f) 80nm Ni/SS, 80 nm TiSi$_2$/SS react with 0.3 sccm methane gas for 180 mins, (g,h) 80nm Ni/SS, 80 nm TiSi$_2$/SS react with 1.0 sccm methane gas for 240 mins.

1. Makkusb, R. C.; Janssenb, A. H. H.; Bruijnb, F. A. d.; Mallant, R. K. A. M. Stainless steel for cost-competitive bipolar plates in PEMFCs. *Fuel Cells Bulletin* 2000, 3, 5-9.

2. Tsuchiya, H.; Kobayashi, O. Mass production cost of PEM fuel cell by learning curve. *International Journal of Hydrogen Energy* 2004, 29, 985-990.

3. Tawfik, H.; Hung, Y.; Mahajan, D. Metal bipolar plates for PEM fuel cell - A review. *Journal of Power Sources* 2007, 163, 755-767.

4. Hermann, A.; Chaudhuri, T.; Spagnol, P. Bipolar plates for PEM fuel cells: A review. *International Journal of Hydrogen Energy* 2005, 30, 1297-1302.

5. Nikam, V. V.; Reddy, R. G.; Collins, S. R.; Williams, P. C.; Schiroky, G. H.; Henrich, G. W. Corrosion resistant low temperature carburized SS 316 as bipolar plate material for PEMFC application. *Electrochimica Acta* 2008, 53, 2743-2750.

6. Lee, S. B.; Cho, K. H.; Lee, W. G.; Jang, H. Improved corrosion resistance and interfacial contact resistance of 316L stainless-steel for proton exchange membrane fuel cell bipolar plates by chromizing surface treatment. *Journal of Power Sources* 2009, 187, 318-323.

7. Wind, J.; Spah, R.; Kaiser, W.; Bohm, G. Metallic bipolar plates for PEM fuel cells. *Journal of Power Sources* 2002, 105, 256-260.

8. Chung, C.-Y.; Chen, S.-K.; Chiu, P.-J.; Chang, M.-H.; Hung, T.-T.; Ko, T.-H. Carbon film-coated 304 stainless steel as PEMFC bipolar plate. *Journal of Power Sources* 2008, 176, 276-281.

9. Fukutsuka, T.; Yamaguchi, T.; Miyano, S.-I.; Matsuo, Y.; Sugie, Y.; Ogumi, Z. Carbon-coated stainless steel as PEFC bipolar plate material. *Journal of Power Sources* 2007, 174, 199-205.

10. Wang, W.-L.; He, S.-M.; Lan, C.-H. Protective graphite coating on metallic bipolar plates for PEMFC applications. *Electrochimica Acta* 2012, 62, 30-35.

11. Novoselov, K. S.; Geim, A. K.; Morozov, S. V.; Jiang, D.; Katsnelson, M. I.; Grigorieva, I. V.; Dubonos, S. V.; Firsov, A. A. Two-dimensional gas of massless Dirac fermions in graphene. *Nature* 2005, 438, 197-200.

12. Novoselov, K. S.; Jiang, Z.; Zhang, Y.; Morozov, S. V.; Stormer, H. L.; Zeitler, U.; Maan, J. C.; Boebinger, G. S.; Kim, P.; Geim, A. K. Room-temperature quantum hall effect in graphene. *Science* 2007, 315, 1379-1379.

13. Geim, A. K.; Novoselov, K. S. The rise of graphene. *Nature Materials* 2007, 6, 183-191.

14.   Novoselov, K. S.; Fal'ko, V. I.; Colombo, L.; Gellert, P. R.; Schwab, M. G.; Kim, K. A roadmap for graphene. *Nature* 2012, 490, 192-200.

15.   Shi, J.-N.; Ger, M.-D.; Liu, Y.-M.; Fan, Y.-C.; Wen, N.-T.; Lin, C.-K.; Pu, N.-W. Improving the thermal conductivity and shape-stabilization of phase change materials using nanographite additives. *Carbon* 2013, 51, 365-372.

16.   Tian, H.; Li, C.; Mohammad, M. A.; Cui, Y.-L.; Mi, W.-T.; Yang, Y.; Xie, D.; Ren, T.-L. Graphene Earphones: An Entertainment for Both Humans and Animals. *ACS Nano* 2014.

17.   Sutter, P. W.; Flege, J.-I.; Sutter, E. A. Epitaxial graphene on ruthenium. *Nature Materials* 2008, 7, 406-411.

18.   Reina, A.; Jia, X.; Ho, J.; Nezich, D.; Son, H.; Bulovic, V.; Dresselhaus, M. S.; Kong, J. Large Area, Few-Layer Graphene Films on Arbitrary Substrates by Chemical Vapor Deposition. *Nano Letters* 2009, 9, 30-35.

19.   Pu, N.-W.; Wang, C.-A.; Sung, Y.; Liu, Y.-M.; Ger, M.-D. Production of few-layer graphene by supercritical CO_2 exfoliation of graphite. *Materials Letters* 2009, 63, 1987-1989.

20.   Jacobberger, R. M.; Arnold, M. S. Graphene Growth Dynamics on Epitaxial Copper Thin Films. *Chemistry of Materials* 2013, 25, 871-877.

21.   Dai, B.; Fu, L.; Zou, Z.; Wang, M.; Xu, H.; Wang, S.; Liu, Z. Rational design of a binary metal alloy for chemical vapour deposition growth of uniform single-layer graphene. *Nature Communications* 2011, 2.

22.   Weatherup, R. S.; Bayer, B. C.; Blume, R.; Ducati, C.; Baehtz, C.; Schloegl, R.; Hofmann, S. In Situ Characterization of Alloy Catalysts for Low-Temperature Graphene Growth. *Nano Letters* 2011, 11, 4154-4160.

23.   Ruemmeli, M. H.; Zeng, M.; Melkhanova, S.; Gorantla, S.; Bachmatiuk, A.; Fu, L.; Yan, C.; Oswald, S.; Mendes, R. G.; Makarov, D.; Schmidt, O.; Eckert, J. Insights into the Early Growth of Homogeneous Single-Layer Graphene over Ni-Mo Binary Substrates. *Chemistry of Materials* 2013, 25, 3880-3887.

24.   Bae, S.; Kim, H.; Lee, Y.; Xu, X.; Park, J.-S.; Zheng, Y.; Balakrishnan, J.; Lei, T.; Kim, H. R.; Song, Y. I.; Kim, Y.-J.; Kim, K. S.; Ozyilmaz, B.; Ahn, J.-H.; Hong, B. H.; Iijima, S. Roll-to-roll production of 30-inch graphene films for transparent electrodes. *Nature Nanotechnology* 2010, 5, 574-578.

25.   Lin, Y.-M.; Jenkins, K. A.; Valdes-Garcia, A.; Small, J. P.; Farmer, D. B.; Avouris, P. Operation of Graphene Transistors at Gigahertz Frequencies. *Nano Letters* 2009, 9, 422-426.

26.   Bunch, J. S.; Verbridge, S. S.; Alden, J. S.; van der Zande, A. M.; Parpia, J. M.; Craighead, H. G.; McEuen, P. L. Impermeable atomic membranes from graphene sheets. *Nano Letters* 2008, 8, 2458-2462.

27.   Nair, R. R.; Wu, H. A.; Jayaram, P. N.; Grigorieva, I. V.; Geim, A. K. Unimpeded Permeation of Water Through Helium-Leak-Tight Graphene-Based Membranes. *Science* 2012, 335, 442-444.

28.   Leenaerts, O.; Partoens, B.; Peeters, F. M. Graphene: A perfect nanoballoon. *Applied Physics Letters* 2008, 93.

29.   Kim, H.; Miura, Y.; Macosko, C. W. Graphene/Polyurethane Nanocomposites for Improved Gas Barrier and Electrical Conductivity. *Chemistry of Materials* 2010, 22, 3441-3450.

30.   Liu, L.; Ryu, S.; Tomasik, M. R.; Stolyarova, E.; Jung, N.; Hybertsen, M. S.; Steigerwald, M. L.; Brus, L. E.; Flynn, G. W. Graphene oxidation: Thickness-dependent etching and strong chemical doping. *Nano Letters* 2008, 8, 1965-1970.

31.   Surwade, S. P.; Li, Z.; Liu, H. Thermal Oxidation and Unwrinkling of Chemical Vapor Deposition-Grown Graphene. *Journal of Physical Chemistry C* 2012, 116, 20600-20606.

32.   Chen, S.; Brown, L.; Levendorf, M.; Cai, W.; Ju, S.-Y.; Edgeworth, J.; Li, X.; Magnuson, C. W.; Velamakanni, A.; Piner, R. D.; Kang, J.; Park, J.; Ruoff, R. S. Oxidation Resistance of Graphene-Coated Cu and Cu/Ni Alloy. *Acs Nano* 2011, 5, 1321-1327.

33.   Sreevatsa, S.; Banerjee, A.; Grebel, H. Graphene as a Permeable Ionic Barrier. In *Graphene and Emerging Materials for Post-Cmos Applications*, Obeng, Y.; DeGendt, S.; Srinivasan, P.; Misra, D.; Iwai, H.; Karim, Z.; Hess, D. W.; Grebel, H., Eds. 2009; Vol. 19, pp 259-264.

34.   Chen, S.; Cai, W.; Piner, R. D.; Suk, J. W.; Wu, Y.; Ren, Y.; Kang, J.; Ruoff, R. S. Synthesis and Characterization of Large-Area Graphene and Graphite Films on Commercial Cu-Ni Alloy Foils. *Nano Letters* 2011, 11, 3519-3525.

35.   Prasai, D.; Tuberquia, J. C.; Harl, R. R.; Jennings, G. K.; Bolotin, K. I. Graphene: Corrosion-Inhibiting Coating. *Acs Nano* 2012, 6, 1102-1108.

36.   Kirkland, N. T.; Schiller, T.; Medhekar, N.; Birbilis, N. Exploring graphene as a corrosion protection barrier. *Corrosion Science* 2012, 56, 1-4.

37.   Kang, D.; Kwon, J. Y.; Cho, H.; Sim, J.-H.; Hwang, H. S.; Kim, C. S.; Kim, Y. J.; Ruoff, R. S.; Shin, H. S. Oxidation Resistance of Iron and Copper Foils Coated with Reduced Graphene Oxide Multilayers. *Acs Nano* 2012, 6, 7763-7769.

38.　　Krishnamurthy, A.; Gadhamshetty, V.; Mukherjee, R.; Chen, Z.; Ren, W.; Cheng, H. M.; Koratkar, N. Passivation of microbial corrosion using a graphene coating. *Carbon* 2013, 56, 45-49.

39.　　Schriver, M.; Regan, W.; Gannett, W. J.; Zaniewski, A. M.; Crommie, M. F.; Zettl, A. Graphene as a Long-Term Metal Oxidation Barrier: Worse Than Nothing. *Acs Nano* 2013, 7, 5763-5768.

40.　　Zhou, F.; Li, Z.; Shenoy, G. J.; Li, L.; Liu, H. Enhanced Room-Temperature Corrosion of Copper in the Presence of Graphene. *Acs Nano* 2013, 7, 6939-6947.

41.　　Hsieh, Y.-P.; Hofmann, M.; Chang, K.-W.; Jhu, J. G.; Li, Y.-Y.; Chen, K. Y.; Yang, C. C.; Chang, W.-S.; Chen, L.-C. Complete Corrosion Inhibition through Graphene Defect Passivation. *Acs Nano* 2014, 8, 443-448.

42.　　Liu, X.; Fu, L.; Liu, N.; Gao, T.; Zhang, Y.; Liao, L.; Liu, Z. Segregation Growth of Graphene on Cu-Ni Alloy for Precise Layer Control. *Journal of Physical Chemistry C* 2011, 115, 11976-11982.

43.　　Gullapalli, H.; Reddy, A. L. M.; Kilpatrick, S.; Dubey, M.; Ajayan, P. M. Graphene Growth via Carburization of Stainless Steel and Application in Energy Storage. *Small* 2011, 7, 1697-1700.

44.　　John, R.; Ashokreddy, A.; Vijayan, C.; Pradeep, T. Single- and few-layer graphene growth on stainless steel substrates by direct thermal chemical vapor deposition. *Nanotechnology* 2011, 22.

45.　　Raman, R. K. S.; Banerjee, P. C.; Lobo, D. E.; Gullapalli, H.; Sumandasa, M.; Kumar, A.; Choudhary, L.; Tkacz, R.; Ajayan, P. M.; Majumder, M. Protecting copper from electrochemical degradation by graphene coating. *Carbon* 2012, 50, 4040-4045.

46.　　Wang, Z. B.; Lu, J.; Lu, K. Chromizing behaviors of a low carbon steel processed by means of surface mechanical attrition treatment. *Acta Materialia* 2005, 53, 2081-2089.

47.　　Yang, L.; Yu, H.; Jiang, L.; Zhu, L.; Jian, X.; Wang, Z. Improved anticorrosion properties and electrical conductivity of 316L stainless steel as bipolar plate for proton exchange membrane fuel cell by lower temperature chromizing treatment. *Journal of Power Sources* 2010, 195, 2810-2814.

48.　　Chae, S. J.; Guenes, F.; Kim, K. K.; Kim, E. S.; Han, G. H.; Kim, S. M.; Shin, H.-J.; Yoon, S.-M.; Choi, J.-Y.; Park, M. H.; Yang, C. W.; Pribat, D.; Lee, Y. H. Synthesis of Large-Area Graphene Layers on Poly-Nickel Substrate by Chemical Vapor Deposition: Wrinkle Formation. *Advanced Materials* 2009, 21, 2328-+.

49.　　Kim, K.; Lee, Z.; Regan, W.; Kisielowski, C.; Crommie, M. F.; Zettl, A. Grain Boundary Mapping in Polycrystalline Graphene. *Acs Nano*

2011, 5, 2142-2146.

50.　　Cho, E. A.; Jeon, U. S.; Hong, S. A.; Oh, I. H.; Kang, S. G. Performance of a 1 kW-class PEMFC stack using TiN-coated 316 stainless steel bipolar plates. *Journal of Power Sources* 2005, 142, 177-183.

51.　　Kelly, M. J.; Egger, B.; Fafilek, G.; Besenhard, J. O.; Kronberger, H.; Nauer, G. E. Conductivity of polymer electrolyte membranes by impedance spectroscopy with microelectrodes. *Solid State Ionics* 2005, 176, 2111-2114.

52.　　Kelly, M. J.; Fafilek, G.; Besenhard, J. O.; Kronberger, H.; Nauer, G. E. Contaminant absorption and conductivity in polymer electrolyte membranes. *Journal of Power Sources* 2005, 145, 249-252.

53.　　LaConti, A. B.; Hamdan, M.; McDonald, R. C. Mechanisms of membrane degradation:Handbook of Fuel Cells. 2003, 648.

54.　　Leenaerts, O.; Partoens, B.; Peeters, F. M. Water on graphene: Hydrophobicity and dipole moment using density functional theory. *Physical Review B* 2009, 79.

55.　　Ferrari, A. C.; Robertson, J. Interpretation of Raman spectra of disordered and amorphous carbon. *Physical Review B* 2000, 61, 14095-14107.